The Astrophysical Journal, 898:139 (19pp), 2020 August 1 https://doi.org/10.3847/1538-4357/ab97b7

Constraining Properties of the Next Nearby Core-collapse Supernova with Multimessenger Signals

MacKenzie L. Warren[1,2,3,8], Sean M. Couch[2,3,4,5], Evan P. O'Connor[6], and Viktoriya Morozova[7]
[1] Department of Physics, North Carolina State University, Raleigh, NC 27695, USA; mlwarre4@ncsu.edu
[2] Department of Physics and Astronomy, Michigan State University, East Lansing, MI 48824, USA
[3] Joint Institute for Nuclear Astrophysics-Center for the Evolution of the Elements, Michigan State University, East Lansing, MI 48824, USA
[4] Department of Computational Mathematics, Science, and Engineering, Michigan State University, East Lansing, MI 48824, USA
[5] National Superconducting Cyclotron Laboratory, Michigan State University, East Lansing, MI 48824, USA
[6] Department of Astronomy and Oskar Klein Centre, Stockholm University, AlbaNova, SE-106 91 Stockholm, Sweden
[7] Department of Physics, The Pennsylvania State University, University Park, PA 16802, USA
Received 2019 December 6; revised 2020 May 12; accepted 2020 May 27; published 2020 July 31

Abstract

With the advent of modern neutrino and gravitational wave (GW) detectors, the promise of multimessenger detections of the next galactic core-collapse supernova (CCSN) has become very real. Such detections will give insight into the CCSN mechanism and the structure of the progenitor star, and may resolve longstanding questions in fundamental physics. In order to properly interpret these detections, a thorough understanding of the landscape of possible CCSN events, and their multimessenger signals, is needed. We present detailed predictions of neutrino and GW signals from 1D simulations of stellar core collapse, spanning the landscape of core-collapse progenitors from 9 to 120 $M_\odot$. In order to achieve explosions in 1D, we use the Supernova Turbulence In Reduced-dimensionality model, which includes the effects of turbulence and convection in 1D supernova simulations to mimic the 3D explosion mechanism. We study the GW emission from the 1D simulations using an astroseismology analysis of the protoneutron star. We find that the neutrino and GW signals are strongly correlated with the structure of the progenitor star and remnant compact object. Using these correlations, future detections of the first few seconds of neutrino and GW emission from a galactic CCSN may be able to provide constraints on stellar evolution independent of preexplosion imaging and the mass of the compact object remnant prior to fallback accretion.

Unified Astronomy Thesaurus concepts: Core-collapse supernovae (304); Gravitational wave astronomy (675); Gravitational wave sources (677); Neutrino astronomy (1100); Supernova neutrinos (1666)

1. Introduction

With the proven success of modern neutrino and gravitational wave (GW) detectors, we have entered the era of truly multimessenger astronomy. Perhaps one of the most exciting prospects for multimessenger astronomy are core-collapse supernovae (CCSNe). CCSNe result from the deaths of massive stars. Stars with zero-age main sequence (ZAMS) masses $M \gtrsim 8\,M_\odot$ will undergo gravitational collapse following their nuclear-burning lifetimes. Once massive stars generate iron cores more massive than the effective Chandrasekhar mass limit (Baron & Cooperstein 1990), pressure support is insufficient to balance gravity and the core begins to collapse. As the core collapses, electron captures generate a tremendous number of electron neutrinos. The inner core of the star rebounds, sending pressure waves through the infalling material and forming an outward moving shock. After core bounce, thermal processes create neutrinos and antineutrinos of all flavors. Ultimately, ∼99% of the gravitational binding energy of the protoneutron star (PNS; ∼a few × 10^{53} erg) is converted into neutrinos and results in a dense neutrino field. As the shock moves through the outer mantle of the iron core, it quickly loses energy to the dissociation of heavy nuclei into free protons and neutrons and soon stalls, becoming an accretion shock.

Although the details of reviving the stalled shock in order to generate a successful explosion are still not fully resolved (Bethe 1990; Janka et al. 2007, 2012, 2016; Janka 2012; Burrows 2013; Lentz et al. 2015; Melson et al. 2015; Müller 2016; Takiwaki et al. 2016; Couch 2017; Cabezón et al. 2018; Ott et al. 2018; O'Connor & Couch 2018a; Burrows et al. 2019), it has become clear that the stalled shock will not be successful in all cases. Some fraction of massive stars will result in "failed" supernovae (O'Connor & Ott 2011; Lovegrove & Woosley 2013; Ertl et al. 2016; Sukhbold et al. 2016, 2018; Adams et al. 2017; Couch et al. 2020)—massive stars that go through core collapse and bounce, only to be unable to generate a successful explosion and resulting in black hole (BH) formation. Although such an event may or may not result in an electromagnetic (EM) transient (Lovegrove & Woosley 2013; Adams et al. 2017; Quataert et al. 2019), "failed" supernovae may have distinct neutrino and GW emission that will allow these events to be detected and distinguished from "successful" supernovae (e.g., Sumiyoshi et al. 2006).

Stellar core-collapse events are prime candidates for multimessenger astronomy: each CCSN event will produce prodigious numbers of neutrinos ($\gtrsim 10^{57}$). To date, supernova neutrinos have only been detected for one event: SN 1987A, from which ∼25 neutrinos were detected over ∼10 s (Arnett et al. 1989). Such an event will be detectable with modern neutrino detectors if it occurs in our Galaxy (Scholberg 2012; Suwa et al. 2019), and potentially beyond with planned future detectors such as Hyper Kamiokande (Scholberg 2012; Himmel & Scholberg 2016; Hyper Kamiokande Proto-Collaboration et al. 2018). aLIGO, Virgo, and KAGRA will

[8] NSF Astronomy & Astrophysics Postdoctoral Fellow.

only be able to detect nearby CCSNe, at a range of $\leqslant$100 kpc (Abbott et al. 2016). GWs from a CCSN have not yet been observed.

The combination of observing neutrinos and GWs will provide multiple views into a single CCSN event. Although ideally GWs, neutrinos, and EM emission will be detected from a single CCSN event, the question remains how much information can be extracted from detection via just one messenger. For example, a CCSN event that occurs in the plane of the galaxy could be entirely obscured from EM detection but will still be detectable in neutrinos and, potentially, GWs. Will we be able to distinguish a "successful" versus "failed" CCSN event without direct detection of EM emission? What can we tell about the progenitor star, explosion mechanism, and remnant compact object from the detection of neutrinos, GWs, or both?

Additionally, as the sensitivities and observation limits of neutrino and GW detectors are improved in coming decades, there is hope of detecting the diffuse supernova neutrino background (Hidaka et al. 2018; Horiuchi & Kneller 2018; Møller et al. 2018; Mathews et al. 2019) or GW background (Buonanno et al. 2005; Kotake et al. 2007; Crocker et al. 2017). However, providing predictions of these backgrounds requires a detailed understanding of the outcomes of CCSN events for all stars with masses and metallicities relevant to the span of cosmic history, as well as reliable predictions of the neutrino and GW emission from such a diverse spectrum of events.

Three-dimensional CCSN simulations will be limited in their use for addressing these questions for the foreseeable future. Such simulations are too computationally expensive to be utilized in sufficiently large sensitivity studies (Nagakura et al. 2019). Spherically symmetric CCSN simulations remain vital to our understanding of CCSN physics and the contributions of CCSNe to galactic chemical evolution. The relatively small computational cost of 1D simulations and the ability to run simulations to late times lend them to these sorts of studies (e.g., progenitor mass (Ugliano et al. 2012; Pejcha & Thompson 2015; Perego et al. 2015; Ertl et al. 2016; Sukhbold et al. 2016, 2018; Ebinger et al. 2019; Couch et al. 2020) or to study nucleosynthesis at late times (Fröhlich et al. 2006a, 2006b, 2006c)).

In this work, we present a study of multimessenger signals—GW and neutrino—from the landscape of massive stellar core collapse using 1D simulations. We utilize the 200 single-star, solar-metallicity, nonrotating progenitors of Sukhbold et al. (2016) with ZAMS masses in the range of 9–120 $M_{\odot}$. Our results are the first detailed predictions for the observable GW and neutrino signals covering the vast majority of the landscape of iron-core, single-star CCSN progenitors.[9]

Additionally, with a large set of simulations, we are able to statistically study the sensitivity of observable neutrino and GW signals to fundamental CCSN physics, as well as correlations between observable signals and progenitor, in a robust manner. Previous works have explored temporal and spatial correlations between the neutrino and GW signals for single CCSN simulations, largely with the aim of measuring the presence of the standing accretion shock instability (SASI) and similar phenomena (Fuller et al. 2015; Camelio et al. 2017; Kuroda et al. 2017; Takiwaki & Kotake 2018; Vartanyan et al. 2019). For rapidly rotating CCSNe, Westernacher-Schneider et al. (2019) found that the characteristic frequency of the GW signal can be imprinted on the neutrino signal and may be detectable for very nearby CCSNe with current facilities such as IceCube.

Torres-Forné et al. (2019a), Sotani & Takiwaki (2016), Sotani & Sumiyoshi (2019), and Müller et al. (2013) found relationships between the GW emission and properties of the progenitor, explosion, and remnant compact object. However, these works were limited to a few progenitor stars and only considered the GW emission. Richers et al. (2017) explored correlations between equation of state parameters with the GW signal at bounce for a variety of nuclear equations of states for rotating CCSNe, and Sotani et al. (2017) found for a single progenitor that detection of two or more GW modes could be used to constrain the nuclear equation of state.

Similarly, there are many works that have studied relationships between the neutrino signal and progenitor and explosion properties. Suwa et al. (2019) proposed that the late-time neutrino emission can be used to constrain the PNS mass for successful CCSN events. Nakamura et al. (2015) used several hundred 2D CCSN simulations to explore correlations between the neutrino luminosity, explosion energy, and progenitor, and Horiuchi et al. (2017) used 2D simulations to determine the relationship between the neutrino signal and core compactness. For a review of constraints from the detection of CCSN neutrinos, we point the reader to Horiuchi & Kneller (2018).

Here, we use correlated neutrino and GW signals to determine the progenitor mass, compact object mass, explosion energy, etc., for any possible CCSN event. Additionally, by considering multimessenger signals in our analysis, we find signals from different messenger sources that may be combined to determine properties of the progenitor star and explosion with more certainty than using a single messenger alone. In Section 2, we discuss the various codes that we use to simulate the CCSNe and resultant neutrino and GW emission. Our results are laid out in Section 3: in Section 3.1, we discuss the observable differences between failed and successful core-collapse events in neutrinos and GWs. The correlations between progenitor and explosion properties and neutrino emission are discussed in Section 3.2, and the GW emission in Section 3.3. In Section 3.4, we consider how signals from different messenger sources may be combined to obtain progenitor properties with increased certainty. We provide our discussion and conclusions in Section 4.

2. Methods

To conduct this study, we start with a massive progenitor star, evolved to the point of core collapse. We then simulate the core-collapse event itself and the resultant explosion (or failure). We use the FLASH multiphysics simulation framework (Fryxell et al. 2000), the details of which are laid out in Section 2.1, to conduct a series of 1D CCSN simulations using the Supernova Turbulence In Reduced-dimensionality (STIR) model (Couch et al. 2020). We simulate the expected neutrino signal as would be observed in a Super Kamiokande–like detector using the SNOwGLoBES code (Scholberg 2012), as detailed in Section 2.2, and calculate the expected GW signal using an astroseismology analysis as discussed in Section 2.3. Finally, in Section 2.4, we present our framework for analyzing the relationships between underlying progenitor and explosion properties with the observable signals.

We use the 200 solar-metallicity progenitor models provided by Sukhbold et al. (2016), with ZAMS masses ranging from 9

[9] Publicly available at [doi:10.5281/zenodo.3667908].

to $120\,M_{\odot}$. These stellar models were created with the KEPLER stellar evolution code, assuming zero rotation and magnetic field, and single-star evolution. We direct the reader to the works of Sukhbold et al. (2016), and references therein, for the details of these models.

2.1. FLASH

We simulated the CCSN events using the FLASH code with the STIR turbulence-driven explosion model (Couch et al. 2020), a new method for artificially driving CCSN explosions in 1D simulations. Turbulence is crucial for understanding the CCSN explosion mechanism, as turbulence may add >20% to the total pressure behind the shock (Couch & Ott 2015) while turbulent dissipation contributes significantly to postshock heating (Mabanta & Murphy 2018), thus aiding in the explosion. Including turbulence results in successful explosions in 1D simulations, replicating the current understanding of the physical explosion mechanism, and reproduces the thermodynamics and composition seen in 3D simulations (Couch et al. 2020).

STIR uses the Reynolds-averaged Euler equations with mixing length theory as a closure to model the effects of turbulence. This model has one primary free parameter, the mixing length parameter, α_{Λ}, which is the usual scaling parameter in mixing length theory (see Cox & Giuli 1968) and scales the strength of the convection. The parameter has been fit to 3D simulations run with FLASH. For details of the STIR model and the fitting to 3D simulations, we point the reader to Couch et al. (2020).

Recently, Müller (2019) has criticized methods for including turbulence in 1D simulations such as STIR and that of Mabanta et al. (2019) for not explicitly enforcing total energy conservation. Müller's principal critique is that the neglect of the turbulent mass flux term in the Reynolds-averaged continuity equation in both STIR and the model of Mabanta et al. (2019) breaks total energy nonconservation. As discussed by Murphy & Meakin (2011) and demonstrated in Murphy et al. (2013), this term is second order in the perturbation and thus expected to be a small correction to the overall mass flux. We have verified this quantitatively in our STIR models, finding that the ignored turbulent mass flux is no larger than about 1% of the background mass flux at any time during our simulations. So, while it is true that precise energy conservation would require inclusion of this turbulent mass flux in the continuity equation, the inclusion of diffusive mixing of energy and composition serves to approximately conserve total energy instead. As explicitly discussed by Couch et al. (2020), and acknowledged by Müller (2019), the turbulent energy in STIR is extracted from the free energy in unstable entropy and composition gradients that drive buoyant convection and turbulence. Therefore, while strict energy conservation is not ensured in STIR, it is approximately conserved depending on the values of the diffusive mixing parameters. Furthermore, all models for driving CCSN explosions in 1D (e.g., Ugliano et al. 2012; Perego et al. 2015; Ertl et al. 2016; Müller et al. 2016; Sukhbold et al. 2016) must abuse some physics, which often can be characterized as implying nonconservation of energy. Take, for instance, the model used by Ugliano et al. (2012), Ertl et al. (2016), and Sukhbold et al. (2016). Here, 1D explosions are achieved by enforcing a rapid contraction of the PNS in order to enhance the emergent neutrino luminosities, yielding explosions. Thus, while some integral resembling the total energy could be constructed and shown to be conserved in this model, the ad hoc prescription for the contraction of the PNS is manifestly inconsistent with the chosen treatment of gravity and equation of state in this model, implying that total energy is not truly conserved.

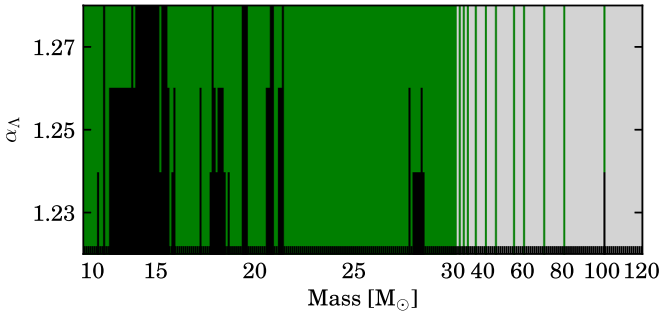

Figure 1. Explodability for supernova progenitors from 9 to $120\,M_{\odot}$ for turbulence strength parameters $\alpha_{\Lambda} = 1.23$–1.27. Green indicates a simulation that did explode successfully, while black indicates a progenitor that does not explode and results in a "failed" supernova event. Gray regions indicated mass regions that were not simulated. The nonmonotonicity of explodability with ZAMS mass has been seen by other groups (O'Connor & Ott 2011; Perego et al. 2015; Sukhbold et al. 2016) and is indicative of the sensitivity of the explosion mechanism to the core structure at the time of collapse.

The purpose of such 1D models is after all to approximate the dynamics of full 3D CCSN simulations, but far more quickly and cheaply. To this end, the true test of the validity of a 1D model should be its ability to reproduce the results of comparable 3D simulations, while making reasonable approximations to the physics of the problem. In Couch et al. (2020), the authors compare the results of STIR to those of Burrows et al. (2019), the largest collection of high-fidelity 3D CCSN simulations in the literature at present. In every single case of the same progenitor model, STIR correctly predicts the key result of explosion or failure compared with the 3D simulations of Burrows et al. (2019). As shown in Couch et al. (2020), other 1D explosion models such as that of, e.g., Ebinger et al. (2019) and Ertl et al. (2016), do not fair that well by this metric. Furthermore, STIR also reproduces the angle-averaged convective and thermodynamic structure of full 3D simulations closely (Couch et al. 2020). The argument that a parameterized 1D model for CCSN explosions must perfectly conserve energy to hold any validity is a fallacious false dilemma.

As was done in Couch et al. (2020), we assume fiducial values for the diffusion coefficients ($\alpha_K = \alpha_e = \alpha_{Y_e} = \alpha_{\nu} = 1/6$) and let the mixing length coefficient α_{Λ} vary between 1.23 and 1.27. $\alpha_{\Lambda} = 0.0$ would correspond to a simulation without convection and turbulence, e.g., the "typical" 1D simulation. Couch et al. (2020) find that the "best-fit" value of α_{Λ}, when comparing to the convection seen in 3D simulations, is about 1.25. Here, we allow this value to vary slightly around the best-fit value also, including simulations with $\alpha_{\Lambda} = 1.23$ and $\alpha_{\Lambda} = 1.27$, to account for uncertainties in the theoretical models, uncertainties in the fitting to the 3D simulation, uncertainties in our understanding of the explosion mechanism, the 1D nature of these simulations, and the multitude of uncertainties in our understanding of stellar evolution such as binarity, rotation, etc. (see, e.g., Clausen et al. 2015).

Figure 1 shows the explodability of the progenitor stars considered in this study, using the STIR model. As has been seen in many previous studies (O'Connor & Ott 2011; Perego et al. 2015; Sukhbold et al. 2016; Couch et al. 2020), the explodability is not simply related to ZAMS mass. Most

notably, STIR predicts a large range of failed explosions and BH formation around $M_{\rm ZAMS} = 13$–$15\,M_\odot$. A gap in explodability is also seen in this mass range by Sukhbold et al. (2018), although it is narrower, and failed explosions are also predicted by 2D and 3D simulations in this mass range as well (Vartanyan et al. 2018; Burrows et al. 2019). This gap would appear to be in tension with the observed masses of red supergiant CCSN progenitors (e.g., Smartt 2009). However, extreme caution should be taken when considering the implications of this because there are substantial sensitivities in the progenitor models (Sukhbold et al. 2018; Sukhbold & Adams 2020) and uncertainties in the ZAMS mass estimation of observationally identified CCSN progenitors (Farrell et al. 2020). For further discussion of the landscape of explodability predicted by the STIR model and how it compares to other codes, we direct the reader to Couch et al. (2020).

The simulations with STIR were run until one of three conditions was met: the shock reached the outer grid boundary (15,000 km), the PNS collapsed to a BH, or a maximum simulation time of 5 s. In principle, there is no reason why explosions cannot occur after 5 s postbounce, but we will consider simulations that reach 5 s without exploding or collapsing to a BH as "failed" CCSNe. However, for much of this work, we will not include these simulations in our study, unless otherwise noted, because we do not truly know the outcome of these simulations and do not have a reliable measure of the time to collapse to a BH.

STIR evolves the turbulent kinetic energy and incorporates corrections due to the turbulent flow directly into the hyperbolic fluxes in the hydrodynamic solver of the FLASH adaptive mesh refinement simulation framework (Fryxell et al. 2000; Dubey et al. 2009). The hydrodynamic solver is a newly implemented (Couch et al. 2020) fifth-order, finite-volume, weighted, essentially nonoscillatory spatial discretization (Shu & Osher 1988; Tchekhovskoy et al. 2007) and a method-of-lines Runge–Kutta time integration (Shu & Osher 1988). We use an Harten–Lax–van Leer contact (HLLC) Riemann solver everywhere except at shocks, where a more diffusive Harten–Lax–van Leer–Einfeldt (HLLE) solver (Toro 2009) is utilized. FLASH treats self-gravity as an approximate general relativistic effective potential (Marek et al. 2009; O'Connor & Couch 2018a). The simulations in this work were run with 10 levels of refinement in a radial domain that extends to 15,000 km, and thus the finest grid spacing is 0.229 km. The maximum allowed level of refinement is limited logarithmically with radius such that $\Delta r/r \lesssim 0.7\%$.

We use an explicit two-moment "M1" neutrino transport scheme with an analytic closure (Shibata et al. 2011; Cardall et al. 2013; O'Connor 2015). The details of the M1 implementation in FLASH can be found in O'Connor & Couch (2018a). FLASH assumes three neutrino flavors for the transport: ν_e, $\bar{\nu}_e$, and ν_x, where ν_x is a combined $\mu-\tau$ neutrino and antineutrino flavor. The simulations in this work include velocity-dependent terms and inelastic neutrino−electron scattering (O'Connor 2015) and 12 logarithmically spaced neutrino energy groups, ranging from 1 to 300 MeV. We use the NuLib neutrino opacity set (O'Connor 2015) that largely matches that of Bruenn (1985), with the addition of corrections due to weak magnetism (Horowitz 2002). We exclusively use the "optimal" equation of state of Steiner et al. (2013) in this work ("SFHo") and assume nuclear statistical equilibrium everywhere in our simulations. The choice of equation of state will most definitely impact both the GW (Richers et al. 2017; Pan et al. 2018) and neutrino emission (Schneider et al. 2019; Yasin et al. 2020), but we leave the exploration of the impact of the equation of state to future work.

Table 1
Detection Channels for a Water Cerenkov Detector and Their Flavor Sensitivities

Channel	Reaction	Neutrino flavor
IBD	$\bar{\nu}_e + p \rightarrow n + e^-$	$\bar{\nu}_e$
ES	$\nu + e^- \rightarrow \nu + e^-$	$\nu_e, \bar{\nu}_e, \nu_x$
$\nu_e - {}^{16}$O	$\nu_e + {}^{16}\mathrm{O} \rightarrow e^- + {}^{16}\mathrm{F}$	ν_e
$\bar{\nu}_e - {}^{16}$O	$\bar{\nu}_e + {}^{16}\mathrm{O} \rightarrow e^+ + {}^{16}\mathrm{N}$	$\bar{\nu}_e$
NC	$\nu + {}^{16}\mathrm{O} \rightarrow \nu + {}^{16}\mathrm{O}$	$\nu_e, \bar{\nu}_e, \nu_x$

2.2. SNOwGLoBES

We use the SNOwGLoBES code (Scholberg 2012) to simulate the observed neutrino signal. SNOwGLoBES[10] is an open-source code for calculating event rates in common neutrino detector materials. Although FLASH produces detailed neutrino fluxes and spectra, we choose to postprocess these fluxes through SNOwGLoBES to ensure that we are focusing on detectable signals, rather than running the risk of finding correlations and coming to conclusions that would not be feasible to detect in current or near-future neutrino detectors. The next galactic CCSN will be observed in more than one detector, and combining the detections from a multitude of detectors will give greater insight as each detector is uniquely sensitive to different energies and neutrino flavors. For the purpose of this analysis, we restrict ourselves to Super Kamiokande. The problem of determining the ideal combination of detectors to interpret the neutrino signal is left to future work.

We use SNOwGLoBES to model the detected neutrino signal in a 32 kton water Cerenkov (Super Kamiokande–like) detector for a CCSN event at 10 kpc, with time bins of 5 ms and energy bins of 0.5 MeV. We have used as input for SNOwGLoBES a pinched Fermi–Dirac neutrino spectrum reconstructed using the parameterization of Keil et al. (2003). We use the "smeared" rates—that is, the neutrino spectrum as a function of energy that will actually be observed in the detector—for each of the relevant channels: inverse beta decay (IBD), electron scattering, charged current interactions with ^{16}O, and neutral current interactions for all flavors. For details of how the event rates are calculated, we refer the reader to Scholberg (2012) and references therein. Table 1 outlines the relevant interaction channels, which are each sensitive to different neutrino flavors and energies. The energy sensitivities and relative count rates of the different channels can also be seen in Figure 2, which shows the time-integrated neutrino spectra to 1 s postbounce for the $28\,M_\odot$ progenitor from Sukhbold et al. (2016), for several values of the turbulence strength parameter α_Λ. The signal will be dominated by the IBD channel, with other channels seeing <170 counts in the postbounce in the first second. Additionally, the neutrino spectra are sensitive to whether or not the progenitor explodes. This progenitor does not explode for $\alpha_\Lambda = 1.23$, but does explode for $\alpha_\Lambda = 1.25$ and 1.27. The neutrino spectrum is harder in all channels for

[10] Available at https://github.com/SNOwGLoBES/snowglobes.

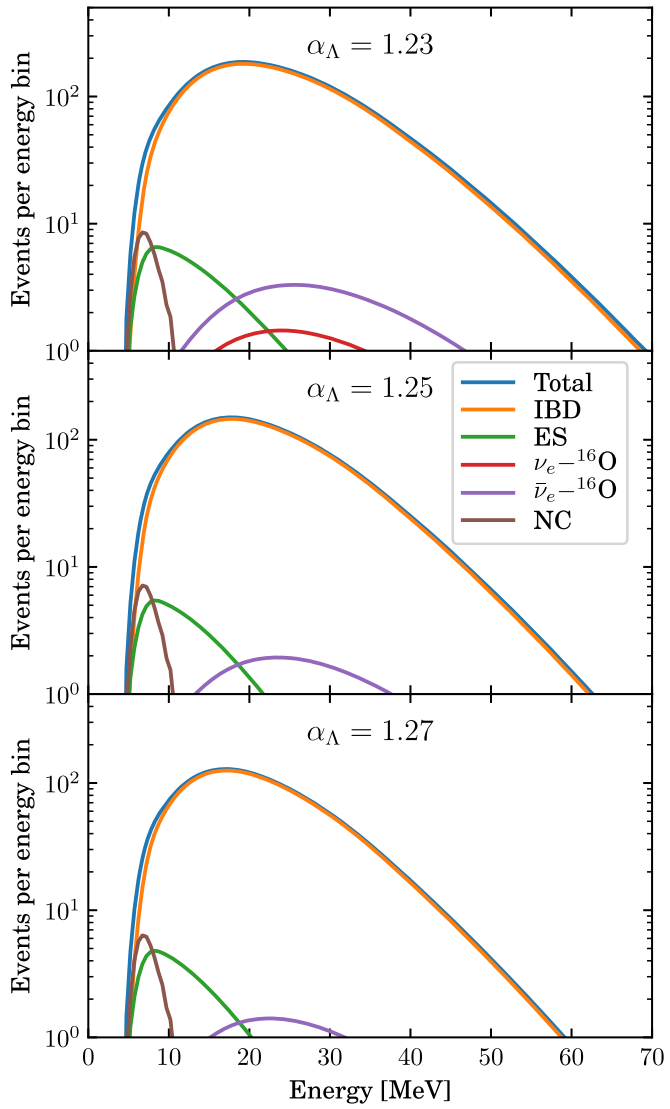

Figure 2. Time-integrated event counts per energy bin out to 1 s postbounce for the 28 $M_\odot$ progenitor from Sukhbold et al. (2016) for turbulence strength parameters $\alpha_\Lambda = 1.23$, 1.25, and 1.27. This progenitor does not explode for $\alpha_\Lambda = 1.23$, but does for higher values of α_Λ. The neutrino energy spectrum is harder and has a higher number of counts for the nonexploding simulation. It is also clear from this figure how the different detection channels are sensitive to different neutrino energies. Count rate is estimated for a 32 kton water Cerenkov detector for a supernova event at 10 kpc for energy bins of 0.5 MeV.

the simulation that does not explode—the observed neutrino mean energy is 24.4 MeV for $\alpha_\Lambda = 1.23$ compared to 22.5 MeV and 21.6 MeV for $\alpha_\Lambda = 1.25$ and $\alpha_\Lambda = 1.27$, respectively. The simulation that does not explode also has a notably higher number of counts—9107 total counts for $\alpha_\Lambda = 1.23$, 6628 for $\alpha_\Lambda = 1.25$, and 5412 for $\alpha_\Lambda = 1.27$. For the successful explosions, the $\nu_e - {}^{16}$O channel will have fewer than one count in the first second, while for the failed explosion it will have several counts.

Given the uncertainties in channel identification in real observing facilities and the large error bars in the count rates for many of these channels—especially those with only a few counts—we limit our discussion from here on to the total neutrino signal, that is, the neutrino signal summed over all channels. As shown in Figure 2, all channels except for the IBD channel will have <10 counts in the first second. Relying on so few counts to make predictions about the progenitor would lead to large uncertainties, given that the statistical uncertainty on 10 counts would be $\sim\sqrt{N} \approx 32\%$. With increased count rates in larger, near-future detectors such as Hyper Kamiokande, it may be possible to loosen this constraint in the future.

We ignore, for the purposes of this study, the effects of neutrino flavor mixing. There are a variety of flavor mixing phenomena that are expected to play a role in a CCSN signal: mixing in the CCSN mechanism due to collective oscillations (Duan et al. 2010), fast oscillations (Sawyer 2005, 2009; Johns et al. 2020; Martin et al. 2020; Morinaga et al. 2020), and Mikheyev–Smirnov–Wolfenstein (MSW) effects (Dighe & Smirnov 2000), as well as mixing due to earth matter effects (Borriello et al. 2012). It is to be expected that neutrino flavor mixing will drastically alter the observed neutrino signals and the expected correlations with progenitor and explosion properties. However, given how little is known about these processes and how they occur in CCSNe, we cannot hope to completely include them here and leave the sensitivities of these correlations to flavor mixing to future work.

2.3. GWs

We use the GW analysis detailed in Morozova et al. (2018) to analyze the GW emission from the PNS. This calculates the eigenfrequencies of the PNS, which are excited by convective downflows and other mechanisms to produce the observed GW emission. Although GW signals are inherently produced by multidimensional effects, the dominant features in the GW signal are due to normal modes of the PNS—particularly the quadrupole ($\ell = 2$) modes (Sotani & Takiwaki 2016; Sotani et al. 2017, 2019; Morozova et al. 2018; Torres-Forné et al. 2018, 2019a, 2019b; Sotani & Sumiyoshi 2019; Westernacher-Schneider et al. 2019).

The analysis laid out in Morozova et al. (2018) requires solving a system of equations including linearized general relativistic hydrodynamics. A bisection method is used to find solutions that satisfy the imposed boundary condition that the pressure perturbation be zero at the PNS surface (assumed to be where $\rho = 10^{10}$ g cm^{-3}). We direct readers to Morozova et al. (2018) for details of how this calculation is done. Morozova et al. (2018) found that the difference between the Cowling and "relaxed" Cowling approximations was negligible at early times ($\lesssim$0.5 s postbounce). We leave the validation of these two approaches to future work and use the Cowling approximation here.

In our analysis, we are predominately interested in the behavior and evolution of the dominant frequency, which can be picked out by comparing to a GW spectrogram found in a 3D simulation (similar to the analysis done using 2D simulations in Morozova et al. 2018). We do not concern ourselves with carefully identifying the specific mode type of this frequency band, but only care about tracking the evolution of the peak frequency, regardless of what mode is generating this frequency. To determine which eigenfrequency corresponds with the peak emission, we compare to the fit formula of Müller et al. (2013),

$$f_{\rm peak} = \frac{1}{2\pi}\frac{GM_{\rm PNS}}{R_{\rm PNS}^2 c}\sqrt{1.1\frac{m_N}{\langle E\rangle_{\nu_e}}}\left(1 - \frac{GM_{\rm PNS}}{R_{\rm PNS}c^2}\right)^2. \quad (1)$$

We determine which eigenfrequency lies closest to this expression, while also enforcing that the peak frequency cannot switch modes until the difference between the mode frequencies is small. Equation (1) was derived from the first

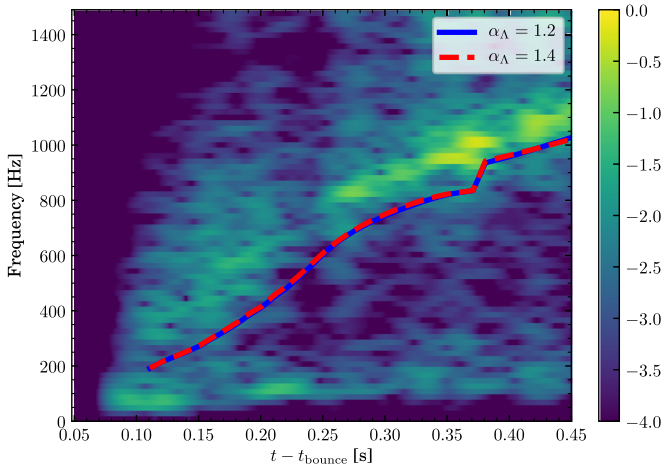

Figure 3. GW spectrogram for 1D and 3D simulations for the $20\,M_\odot$ progenitor of Farmer et al. (2016). The background 3D spectrogram is from simulations run in O'Connor & Couch (2018a). The blue line indicates the frequency evolution for the peak GW frequency found with the 1D GW code for the same progenitor, run with STIR using $\alpha_\Lambda = 1.2$, and the red line is the frequency evolution found in 1D with $\alpha_\Lambda = 1.4$. Because there is little variation in the modes with α_Λ, it is clear which mode is the dominant GW mode when comparing to the 3D spectrogram.

<1 s postbounce of the 2D simulations. Therefore, we do not trust it to properly approximate the peak frequency evolution at several seconds postbounce. At later times, we assume that the peak frequency does not switch modes after ∼0.5 s postbounce, which seems to be an adequate assumption, as the modes diverge significantly at later times. We do not track the evolution of the mode prior to 100 ms postbounce because, early postbounce, there are many overlapping modes and eigenfrequencies, making it difficult to determine which frequency is the correct one to consider here. The bounce signal may contain a wealth of information about the progenitor, rotation, equation of state, and numerous other quantities (Richers et al. 2017; Pajkos et al. 2019). However, capturing the bounce signal is beyond what is feasible with 1D simulations, and we do not concern ourselves with it here.

We verify that we are able to pick out the peak frequency by comparing 1D STIR simulations of a $20\,M_\odot$ progenitor to the 3D simulations done in O'Connor & Couch (2018a), as shown in Figure 3. These simulations are for a $20\,M_\odot$ progenitor created using the MESA stellar evolution code (Paxton et al. 2011, 2013, 2015; Farmer et al. 2016), with the SFHo equation of state and M1 neutrino transport.

The turbulence strength parameter will affect the GW emission because the turbulence will change the PNS structure by diffusing lepton fraction, including the temperature, and energy in the PNS. Additionally, turbulence will change the amount of fallback and accretion onto the PNS, thus changing its mass. However, for early-time (<0.5 s) postbounce for the simulations shown in Figure 3, with $\alpha_\Lambda = 1.2$, which does not explode, and $\alpha_\Lambda = 1.4$, there is negligible difference between the peak frequency evolution at early times and a ∼11% difference between the frequencies at about 2 s postbounce. Thus, we are able to pick out the dominant frequencies for all of the progenitors and turbulence strength parameters α_Λ, assuming that this mode does not change dramatically between progenitors (Müller et al. 2013; Yakunin et al. 2015; Morozova et al. 2018; Torres-Forné et al. 2019a). The switch from one eigenfrequency mode to another is apparent in both the $\alpha_\Lambda = 1.2$ and 1.4 simulations at about 0.40 s postbounce. Because the eigenmodes are discrete, this switch in modes appears as a sudden jump in the peak frequency. In multidimensional simulations, as is apparent in the spectrogram from the 3D simulation, the peak frequency is smooth and continuous and does not show a sudden jump. This is likely because, as the peak frequency approaches the change in modes, both eigenmodes are simultaneously excited for some time, resulting in a smooth transition between frequencies.

It is worth noting that, while this analysis can reproduce the frequencies of the GW emission from the PNS, it fails to fully capture the GW emission seen in multidimensional simulations because it does not model the relative strength of each mode or the energy in each mode. For example, the amplitude of the GW signal will be set by the convection, SASI, and other nonspherical hydrodynamic effects above the PNS (Kuroda et al. 2016; O'Connor & Couch 2018b; Andresen et al. 2019; Pajkos et al. 2019; Radice et al. 2019). There is some indication that the GW energy can be derived from the turbulent energy (Radice et al. 2019), but we leave such an analysis to future work. We focus instead entirely on the evolution of the peak frequency of the GW emission without concerning ourselves with the relative strength of this frequency or the spectrum of different frequency bands. Thus, the GW signals produced in this work, and by 1D models in general, cannot be used as exact predictions of GW signals from CCSNe. However, knowledge of the peak frequency is sufficient for exploring the relationship between the GW emission and other physics of the supernova environment.

2.4. Correlations

We analyze the simulated neutrino and GW signals described above for correlations between observable quantities and fundamental physics parameters and properties of the progenitor stars. Given the large sample of simulations we include here (600), we are uniquely situated to explore statistical correlations in a way that has been inaccessible to many previous studies due to small numbers or use of more approximate neutrino physics. We take our inspiration for using correlation matrices to explore relationships between simulation properties from Richers et al. (2017), which used correlation matrices to explore the relationship between equation of state parameters and the GW signal at bounce in rotating CCSNe.

We calculate the Pearson product–moment correlation coefficient using the Python SciPy package (Jones et al. 2001). The Pearson coefficient r is a measure of the linear correlation between two variables and is calculated by the covariance of the two variables of interest, divided by their standard deviations,

$$r = \frac{\sum_i (x_i - \bar{x})(y_i - \bar{y})}{\sqrt{\sum_i (x_i - \bar{x})^2}\sqrt{\sum_i (y_i - \bar{y})^2}} \quad (2)$$

for variables x and y. A correlation coefficient value of $r \sim 1$ indicates an extremely strong positive correlation, a correlation coefficient of $r \sim -1$ indicates an extremely strong negative correlation, and a coefficient value of $r \sim 0$ indicates that there is no correlation between the variables. For the purposes of this work, we consider a strong correlation to be $|r| \gtrsim 0.5$, a

Table 2
Parameters Considered in Correlations

Quantity	Parameters
Stellar structure	ZAMS mass
	Mass at time of core collapse
	Stellar radius at time of core collapse
	Core compactness ($\xi_{2.5}$)
	Iron-core mass
	Ertl parameters μ and M_4 (Ertl et al. 2016)
Explosion dynamics	Explosion energy
	Mass accretion rate
	Heating rate in the gain region
	Time of the onset of explosion
	PNS radius
Neutrino signal	Maximum counts in one 5 ms time bin
	Timescale to reach 90% of the total counts
	Various functional fits of the mean energy & counts evolution
GW signal	Various functional fits of the peak frequency evolution
	Timescale to reach 90% of the maximum peak frequency
	Peak frequency at various times postbounce

Note. Quantities not included in the main text were found to have weak or no correlation with multimessenger signals or were describing similar physics to parameters that were used.

moderate correlation to be $0.3 \lesssim |r| \lesssim 0.5$, and $|r| \lesssim 0.3$ to be a poor correlation. Note that the r value does not indicate the slope of the relationship between the data but is a measure of the strength of the correlation.

This method of using the Pearson r value will not distinguish between "noisy" linear data and data related in nonlinear ways—for example, a noisy linear relationship can have the same r value as a tight, quadratic relationship. It is unlikely that all, or even most, quantities of interest will be linearly correlated in such a complex environment as a CCSNe. Considering linear correlations will provide a significant first step and, as we will see, be sufficient to uncover insightful and significant relationships between observable quantities and progenitor and explosion properties (see Torres-Forné et al. 2019a). More complex analysis to determine nonlinear correlations is left for future work.

In conducting this analysis, we consider numerous variables and parameterizations of the progenitor, explosion, and observable properties. There are countless quantities that could be considered here. We have explored numerous parameters of the neutrino signal, progenitor, and explosion. Many of these parameters were found to have little relationship with the physics that we are interested in exploring here, such as the radius of the star at the time of collapse, or are intimately related with quantities that we do consider. For example, we will use the core compactness $\xi_{2.5}$ (O'Connor & Ott 2011),

$$\xi_{2.5} = \left. \frac{2.5\ M_\odot/M_\odot}{R(M_{\rm bary} = 2.5\ M_\odot)/1000\ \ {\rm km}} \right|_{t=t_{\rm collapse}}, \quad (3)$$

as a measure of the structure of the progenitor core at the time of collapse. Similar parameters, such as the parameters defined by Ertl et al. (2016), measure essentially the same thing and would have very similar relationships with observable quantities. Other parameters are known to be unrelated from previous works; for example, the ZAMS mass has little relationship with the explosion and physics in the core (O'Connor & Ott 2011; Ugliano et al. 2012; Ertl et al. 2016; Sukhbold et al. 2016; Couch et al. 2020) and the peak luminosity is largely insensitive to the ZAMS mass (Liebendörfer et al. 2004; O'Connor & Ott 2013). For sake of clarity and brevity, we will only show variables here that showed strong (anti)correlations with observables. For a list of parameters considered, please see Table 2.

3. Results

3.1. Distinguishing Failed versus Successful Events

Perhaps the simplest "observable" feature from the death of a massive star is determining whether or not the core collapse results in a successful supernova event or a failed supernova and collapse to BH. The critical difference between these possibilities is of course the occurrence of an EM transient consistent with a CCSN. However, there may be cases where such a transient is not visible if it occurs toward the galactic center. Also, given that the EM transient occurs ∼hours to days after the GW and neutrino emission, one might hope to determine the outcome of the core collapse without waiting for shock breakout.

There are a few key observable differences between the neutrino and GW emission from successful and failed events. Figure 4 shows the shock radius, neutrino luminosity, neutrino mean energy, peak GW frequency, and baryonic PNS mass versus time postbounce for failed and successful CCSN events for several progenitor masses. These progenitors were chosen because they span the range of ZAMS mass (13, 28, and 100 $M_\odot$) and core compactness (0.058, 0.281, and 0.244 respectively) and have a "critical" α_Λ value between 1.23 and 1.27. For a given progenitor, there is a critical α_Λ value at which it starts to explode, the value of which depends sensitively on the progenitor (Couch et al. 2020).

The most obvious distinction between successful and failed events will be an abrupt "stop" in the neutrino and GW signal. The GW emission should stop abruptly, similar to what is seen in simulations of BH formation for binary neutron star mergers (for example see Radice et al. 2017). When the cooling PNS collapses to a BH, neutrino emission should end quite promptly as well. Thus, a sharp ending of both the neutrino and GW emission will be a clear indicator of a failed explosion.

In our 1D models, the neutrino luminosity and mean energy drop off at the time that explosion sets in, as evident in comparing the neutrino emission to the shock radius. This is due to the fact that accretion onto the PNS stops once the explosion sets in and can no longer serve as a source of neutrinos, leaving only the cooling PNS as a neutrino source. One could imagine using the observation of such a drop-off as a marker of the time of the onset of explosion. However, this would depend on being able to distinguish a drop-off in neutrino emission due to the onset of explosion from a drop-off due to the structure of the progenitor star, e.g., the accretion of the Si/O interface through the shock (Seadrow et al. 2018), although there are some indications that the accretion of the Si/O interface is tied to the explodability (Fryer 1999; Murphy & Burrows 2008; Summa et al. 2016; Vartanyan et al. 2018). For example, the 13 $M_\odot$ simulations in Figure 4 do not explode for $\alpha_\Lambda = 1.23$ and $\alpha_\Lambda = 1.25$. Yet, there is still a "drop" in the neutrino luminosities at ∼0.25 s postbounce due to the

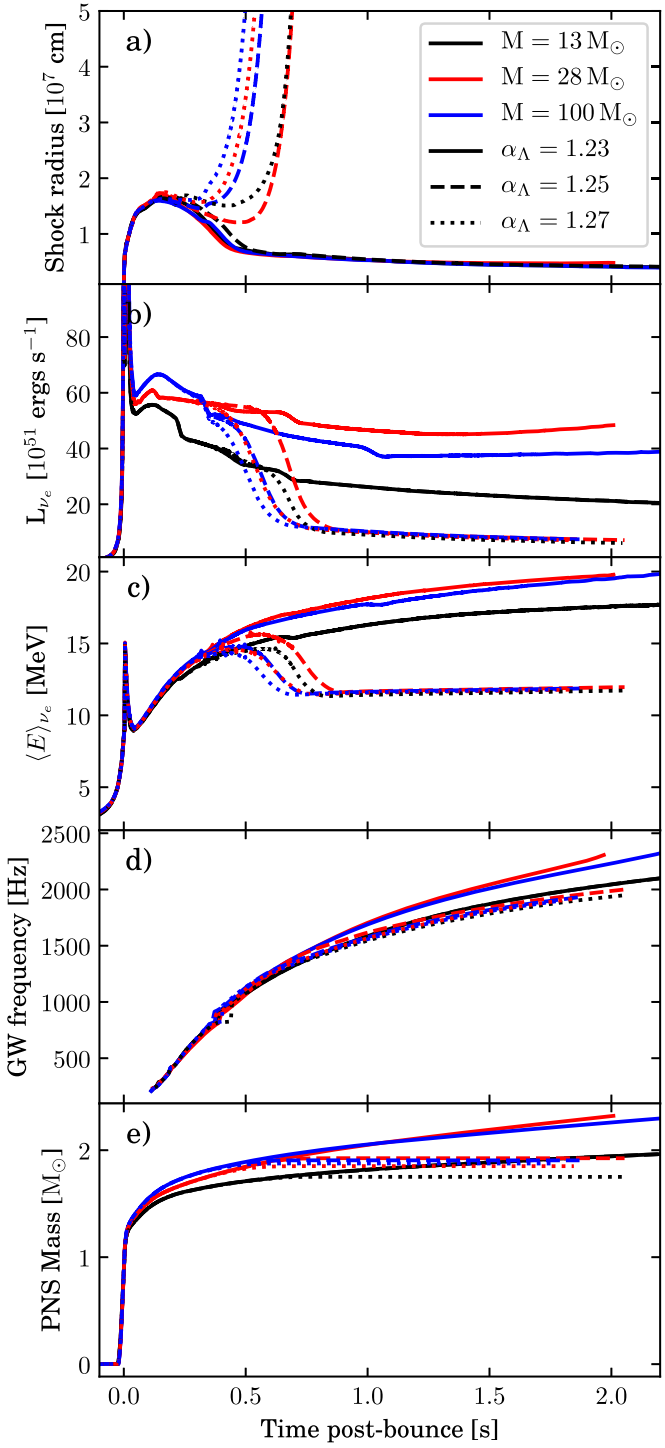

Figure 4. Shock radius, PNS mass, and multimessenger signals vs. time postbounce for various progenitors and turbulence strength parameters. Panel (a) shows the shock radius, panel (b) shows electron neutrino luminosity, panel (c) shows the electron neutrino mean energy, panel (d) shows the dominant GW frequency, and panel (e) shows the PNS (baryonic) mass. The black lines are for a 13 $M_\odot$ progenitor, the red for 28 $M_\odot$, and blue for a 100 $M_\odot$ progenitor. The solid lines are a turbulence strength parameter of $\alpha_\Lambda = 1.23$, the dashed lines show $\alpha_\Lambda = 1.25$, and the dotted lines $\alpha_\Lambda = 1.27$. The 13 $M_\odot$ progenitor has a critical α_Λ value of 1.27 at which it begins to explode. The 28 $M_\odot$ and 100 $M_\odot$ progenitors have a critical α_Λ value of 1.25. It may be possible to tell when explosion sets in by the sharp drop-off in the neutrino luminosity and mean energy, which corresponds to the diverging GW signals for each progenitor. Note that, although not plotted here, there will be GW emission prior to 200 ms postbounce.

structure of the progenitor star. A good diagnostic to distinguish between the onset of explosion and accretion of the Si/O shell interface seems to lie in the neutrino average energies. The average energies, shown in panel (c) of Figure 4, do not show the same dramatic drop as the neutrino luminosities at the accretion of composition interfaces, only at the onset of explosion. Thus, observation of a sharp drop-off in both the neutrino luminosity and mean energy could be indicative of the onset of explosion. This is in agreement with the results of Sumiyoshi et al. (2006, 2008), where they found that the increased accretion in failed CCSN events leads to higher neutrino luminosities and average energies after the neutronization burst relative to a successful explosion.

Further work must be done to explore this phenomenon thoroughly in multidimensional models. The drop-off in accretion at the onset of explosion is stronger in 1D simulations than in 2D or 3D, because multidimensional models allow for continued accretion onto the PNS surface after the explosion begins, but this feature appears to still be present in most multidimensional simulations (O'Connor & Couch 2018b; Burrows et al. 2019; Müller et al. 2019). It remains unexplored how these observable features depend on the line of sight, and perhaps more importantly, whether the line of sight is aligned or misaligned with a downflow of accreted material.

There is also a divergence in the evolution of the peak GW frequency, shown in panel (d) of Figure 4, at the onset of explosion. As a given progenitor reaches its critical α_Λ value, at which it starts exploding, the peak GW frequency diverges at the time of the onset of explosion and asymptotes to lower frequencies than in the case of a failed supernova event. This is a much less dramatic effect than that seen in the neutrino signal. It will likely be difficult to distinguish this effect given the differences in peak GW behavior between progenitors—the failed event for the 13 $M_\odot$ progenitor is difficult to distinguish from the successful explosions of the 28 and 100 $M_\odot$ progenitors. The divergence of the GW signals is related to the PNS structure and evolution. Panel (e) in Figure 4 shows the evolution of the baryonic PNS mass for these simulations. The same divergence occurs in the PNS masses with the onset of explosion. This is due to the fact that, as noted above, in 1D, accretion shuts off at the onset explosion, thereby halting the growth of the PNS mass. This steeper rise in the GW frequency for failed CCSNe was also seen by Sotani & Sumiyoshi (2019).

The success, or failure, of a nearby CCSN event should be imprinted on the neutrino and GW signals long before EM emission is visible. Failed events result in a sharp end to the neutrino and GW emission in the first few seconds. Successful events have a drop in the neutrino counts and mean energy at the time that explosion sets in, but have continued neutrino and GW emission. From now on, we consider "successful" and "failed" CCSNe as separate populations. As we will see, the relationship between observable parameters and information about the progenitor are very different in the two cases due to the different physics driving the creation of neutrinos and GW signals in these environments.

3.2. Neutrino Signals

We consider the neutrino signal that would be observed in a Super Kamiokande–like 32 kton water Cerenkov detector for a CCSN event at 10 kpc, as simulated using the

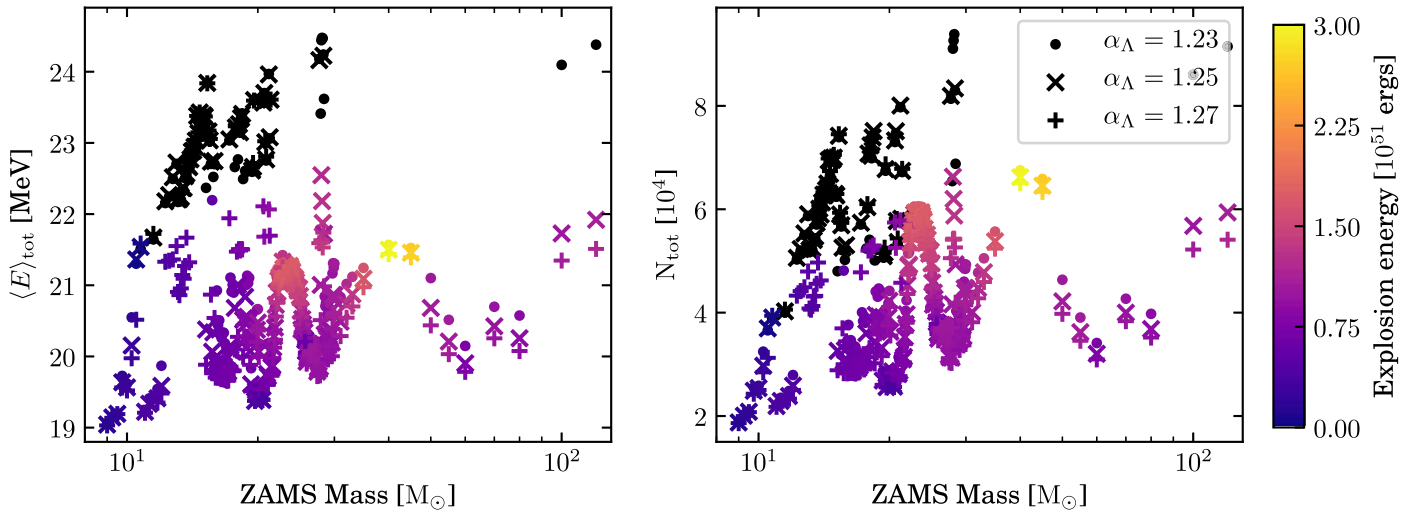

Figure 5. Left panel shows the time-integrated neutrino mean energy, $\langle E \rangle_{\rm tot}$, and the right panel shows the time- and energy-integrated counts, $N_{\rm tot}$, to 1 s postbounce and summed over all channels, vs. ZAMS mass. Energies and count rates were calculated assuming a 32 kton water Cerenkov detector for a CCSN event at 10 kpc. The color scales with the explosion energy, and black indicates a simulation that did not explode, including those that ran to 5 s postbounce without collapsing to a BH. The symbols indicate the turbulence strength parameter α_Λ. Neither average energy nor neutrino counts show any simple relationship with the ZAMS mass. There is a somewhat progenitor-dependent dividing line in average energy that separates successful explosions from those that fail. However, explosion energy appears to be more strongly related to the neutrino counts.

SNOwGLoBES code (Scholberg 2012). Using SNOwGLoBES, we are able to obtain the time evolution of the observed neutrino spectra in the various channels, as listed in Table 1.

In order to simplify the comparison between simulations, we do not consider here the time evolution of the neutrino emission. There are two parameters that we consider: the mean energy $\langle E_{\rm tot} \rangle$ of the time-integrated detected neutrinos and the time- and energy-integrated number of neutrinos detected, $N_{\rm tot}$, or counts, in all channels, integrated to 1 s postbounce. We note that for the former, due to the energy dependence of the neutrino cross sections in water, the mean detected energy is not the same as the mean energy of the emitted spectrum (i.e., the values plotted in Figure 4). Although we have chosen to integrate out to 1 s postbounce, one should note that, for successful CCSN events, the neutrino signal may be detectable for tens or hundreds of seconds, and the late-time signal will contain information about the PNS mass and structure (Roberts et al. 2012; Suwa et al. 2019). There are many indications though that significant information about the progenitor star and explosion can be inferred from the first second or less of the neutrino signal (e.g., see Horiuchi et al. 2017). We find that there were no significant correlations between basic measures of the time evolution, such as timescales, slopes, and fits of the neutrino quantities. Using time-integrated quantities has the added benefit of decreasing potential observational uncertainties—the higher the number of counts being considered, the smaller the relative error. This will allow for a more reliable relationship to be established between observable quantities and the underlying progenitor structure and explosion.

We can now ask whether we can distinguish features of the supernova progenitor using these time-integrated neutrino quantities. Figure 5 shows the mean energy and counts in all channels for progenitors with ZAMS mass between 9 $M_\odot$ and 120 $M_\odot$ and turbulence strength parameter α_Λ between 1.23 and 1.27, with the explosion energy indicated by the color. As has been seen with other CCSN observables, such as the explodability shown in Figure 1, the neutrino mean energy and counts do not vary monotonically with ZAMS mass. The neutrino mean energy, similar to the explodability, shows a behavior with ZAMS mass similar to the compactness parameter $\xi_{2.5}$ (O'Connor & Ott 2011), as defined in Equation (3). This is perhaps unsurprising, as the neutrino emission comes directly from the core of the CCSN event and is not significantly impacted by the ZAMS mass or outer envelope.

The average detected neutrino energy, shown in the left panel of Figure 5, and neutrino counts, in the right panel, show a general decreasing trend with increasing turbulence strength for a given progenitor. This is consistent with previous work done that shows decreasing neutrino average energies with turbulence strength in the STIR model (Couch et al. 2020). The rate, however, at which the mean energy and counts decrease with turbulence strength varies. This is related to the explodability and critical α_Λ value of each particular progenitor. The neutrino mean energy and counts drop dramatically at the critical α_Λ value for a given progenitor—that is, they drop dramatically in simulations that explode successfully compared to simulations that fail. This can be seen most clearly for the 100 and 120 $M_\odot$ progenitors, which have a critical α_Λ value of 1.25 at which they begin to explode. However, this is not a reliable means to distinguish between successful and failed events because the "dividing line" in mean energy and counts between failed and successful CCSNe varies dramatically between progenitors.

We can begin to explore the deeper connections between these two detectable neutrino parameters—mean energy and counts—with underlying properties of the progenitors, explosion mechanism, and remnant compact object. Figure 6 shows the correlation strength for simulations that explode successfully. We compare here the behavior of the neutrino emission with the core compactness ($\xi_{2.5}$), the PNS mass ($M^b_{\rm PNS}$) at 1 s postbounce, and the explosion energy ($E_{\rm expl}$). The PNS mass considered throughout this work is the baryonic mass. The core compactness ($\xi_{2.5}$) is strongly correlated with the number of neutrino counts in all channels ($N_{\rm tot}$), as was also seen by

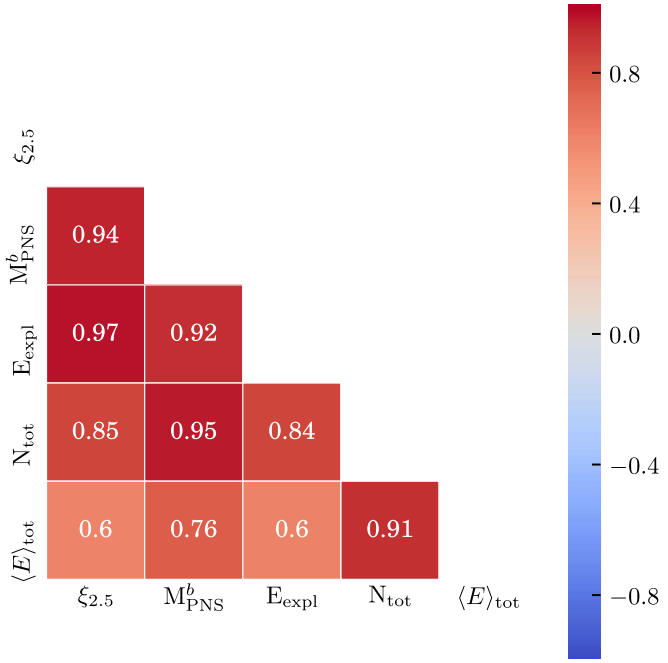

Figure 6. Correlation matrix for observable neutrino quantities and underlying properties of the progenitor and explosion for simulations that successfully explode. The quantities considered are core compactness ($\xi_{2.5}$), baryonic PNS mass ($M^b_{\rm PNS}$) at 1 s postbounce, explosion energy ($E_{\rm expl}$), time- and energy-integrated neutrino counts ($N_{\rm tot}$) in all channels, and the time-integrated average neutrino energy in all channels ($\langle E\rangle_{\rm tot}$). The lower-left half shows the correlation strength, ranging from −1 to 1, as indicated by the color and number in each of the squares.

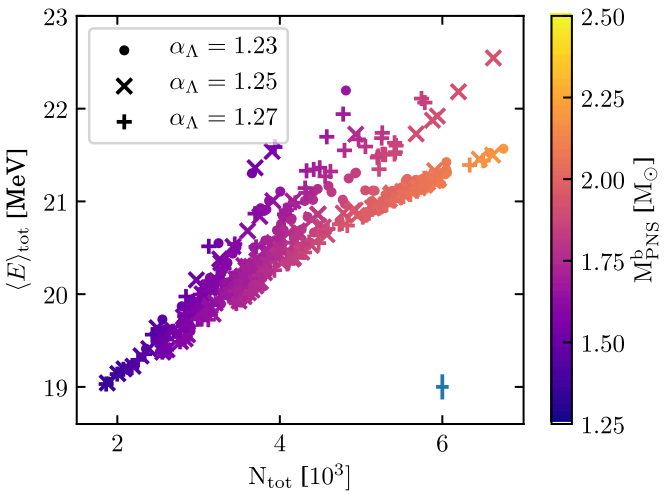

Figure 7. The plane of the neutrino mean energy ($\langle E\rangle_{\rm tot}$) of the time-integrated observed neutrino spectrum vs. time- and energy-integrated neutrino counts ($N_{\rm tot}$), in all channels out to 1 s postbounce, for simulations that explode successfully. Count rates are simulated for a 32 kton water Cerenkov detector for a CCSN event at 10 kpc. The PNS baryonic mass $M^b_{\rm PNS}$ at 1 s postbounce is indicated by the color bar. Symbols indicate the turbulence strength parameter α_Λ used in the simulation. The blue shows an example of the observational error bars for measuring the total number of counts and mean energy at 10 kpc.

Horiuchi et al. (2017). The core compactness is related to the total gravitational energy released in the collapse and thus, the total neutrino energy released (O'Connor & Ott 2013). The PNS mass at 1 s postbounce ($M^b_{\rm PNS}$) is also strongly correlated with the number of neutrino counts in all detection channels, as shown in the second column of Figure 6.

Explosion energy is also strongly correlated with the number of neutrino counts. The explosion energy is highly sensitive to the amount of neutrino heating in the gain region behind the shock—and the heating rate scales with the neutrino energies and counts. The count rate in the detector is similarly sensitive to these quantities, given that the detector will be more sensitive to higher energy neutrinos. Thus, the count rate in the detector may give significant insight into the neutrino heating occurring in the CCSN environment. The explosion energy is less strongly correlated with the neutrino mean energy, $\langle E\rangle_{\rm tot}$, than with the neutrino counts. This is also somewhat apparent in Figure 5. The "peak" in the explosion energy around the ZAMS mass of 40 $M_\odot$ is also a peak in the number of counts for simulations that do explode successfully, but is less pronounced of a peak in the neutrino mean energy, $\langle E\rangle_{\rm tot}$.

Given the strong correlations between the neutrino counts and quantities that cannot be directly observed, such as the PNS mass, it may then be possible to obtain these progenitor and explosion properties with careful observations of the neutrino emission. Figure 7 shows the plane of neutrino counts and average neutrino energy at 1 s after bounce for all of our simulations that explode successfully, with the PNS mass indicated by the color. There is a clear trend in PNS mass with neutrino counts and mean energy, in concordance with the high values of the correlation parameter found earlier.

For a fixed number of neutrino counts, there is a counter-intuitive trend that increasing mean energy corresponds with decreasing PNS mass, contrary to the positive correlation found in these quantities in Figure 6. This can be understood as being due to competing effects. The number of neutrino counts is integrated over the first second postbounce and, for a given, fixed number of neutrino counts, there are several ways to generate that number—a high luminosity over a shorter period, or lower luminosity over the full 1 s. Simulations that result in a higher PNS mass tend to have a higher compactness and explode more quickly, thus having a higher luminosity but over a shorter period until the explosion sets in ($t_{\rm expl} < 1$ s). The mean energy, however, is initially quite similar for all of these simulations, until it drops at the onset of explosion. Thus, the mean energy integrated over 1 s postbounce will be lower for simulations that explode more quickly. For a fixed number of neutrino counts, a higher PNS mass will correspond to a lower neutrino mean energy. It is clear that the CCSN environment is not set or discernible using a single parameter alone, be it core compactness, PNS mass, etc. There are competing effects that lead to a great deal of complexity in these simulations.

The lack of scatter despite using several values of the turbulence strength parameter α_Λ indicates that this relationship is relatively insensitive to the assumptions and uncertainties in our underlying 1D supernova model. Significantly, this is a measure of the PNS mass at 1 s postbounce as the explosion is occurring and before fallback accretion. Such a measurement would provide a means to "watch" the evolution of the PNS and help determine the role of fallback accretion in the CCSN environment. A similar process can be applied to determining other progenitor and explosion parameters, such as the core compactness and explosion energy.

In Table 3, we provide linear fits between the observable neutrino parameters and the core compactness, PNS mass, and explosion energy for successfully exploding CCSN events, of a

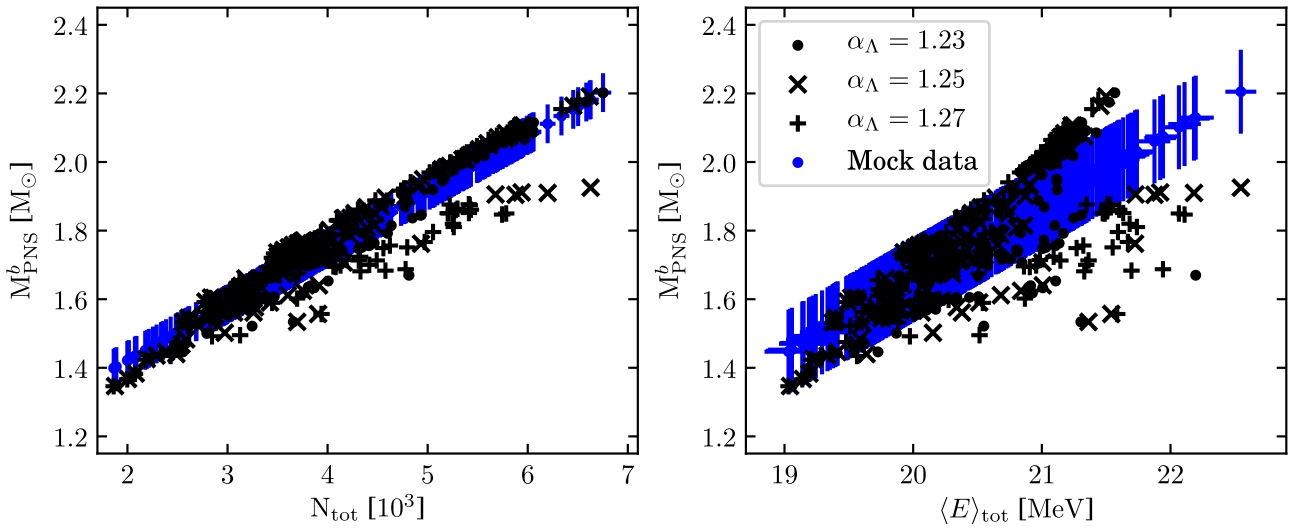

Figure 8. Left panel shows the PNS baryonic mass (M^b_{PNS}) vs. time- and energy-integrated neutrino counts in all channels out to 1 s postbounce (N_{tot}). The right panel shows the PNS mass vs. neutrino mean energy of the time-integrated observed neutrino spectrum in all channels out to 1 s postbounce ($\langle E\rangle_{tot}$). Black points are the simulation results for $\alpha_\Lambda = 1.23-1.27$. Blue points show the PNS mass found using the fitted relationship from Table 3. Fitted points include the statistical error in the measurement and standard deviation of the residuals. It is clear that, for a distance of 10 kpc at least, it is advantageous to determine the PNS mass from the number of counts, rather than the mean energy. However, using the number of counts in this determination depends on having an accurate measurement of the distance.

Table 3
Linear Fits to Observable Neutrino Parameters for Successfully Exploding CCSN Events for the Core Compactness, $\xi_{2.5}$, PNS Mass at 1 s Postbounce, M^b_{PNS}, and Explosion Energy, E_{expl}

Parameter	$C_{N_{tot}}$	$C_{\langle E\rangle_{tot}}$	D	R^2
$\xi_{2.5}$ (unitless)	$(8.662 \pm 0.255) \times 10^{-5}$	⋯	$(-1.272 \pm 0.107) \times 10^{-1}$	0.714
	⋯	$(1.011 \pm 0.063) \times 10^{-1}$	-1.845 ± 0.129	0.361
M^b_{PNS} ($M_\odot$)	$(1.643 \pm 0.024) \times 10^{-4}$	⋯	1.093 ± 0.010	0.911
	⋯	$(2.156 \pm 0.009) \times 10^{-1}$	-2.656 ± 0.175	0.582
E_{expl} (10^{51} erg)	$(3.255 \pm 0.096) \times 10^{-4}$	⋯	$(-4.380 \pm 0.405) \times 10^{-1}$	0.712
	⋯	$(3.811 \pm 0.236) \times 10^{-1}$	-6.921 ± 0.483	0.362

Note. These coefficients are for the functional fit of the form $y = C_{N_{tot}} N_{tot} + C_{\langle E\rangle_{tot}} \langle E\rangle_{tot} + D$, with the mean energy, $\langle E\rangle_{tot}$, measured in MeV. R^2 is the correlation coefficient between the data and the fit, and measures the quality of the fit. Note that these fits assume a distance of 10 kpc and thus the number of counts will have to be scaled accordingly for CCSN events at other distances.

functional form

$$y = C_{N_{tot}} N_{tot} + C_{\langle E\rangle_{tot}} \langle E\rangle_{tot} + D, \quad (4)$$

where $C_{N_{tot}}$ is the coefficient to the number of neutrino counts N_{tot}, which can be found in Table 3, and $C_{\langle E\rangle_{tot}}$ is the coefficient to the neutrino mean energy $\langle E\rangle_{tot}$. These fits can be used to estimate progenitor and explosion properties from a galactic supernova event and require just the first second of neutrino detections. These fits assume a distance of 10 kpc. We have not included fits using both the number of neutrino counts, N_{tot}, and mean energy $\langle E\rangle_{tot}$ because, due to the stronger correlation with counts than mean energy, the coefficients of the best fit for the mean energy is essentially zero and the fit relies on the counts alone.

Such a detection and early parameter estimation will provide insight into the progenitor star without requiring preexplosion imaging. Perhaps most significantly, measurement of the core compactness, $\xi_{2.5}$, will provide insight into the structure and core of the progenitor star that can be compared with those found with preexplosion imaging. An additional measurement constraining the core structure will put significant constraints on stellar evolution models and the evolutionary tracks of CCSN progenitors.

Figure 7 also includes an example of the purely statistical error bars for the measurement of the number of neutrino counts and mean energy (but assuming no error on the individual neutrino energy measurements, which varies by detector), and Figure 8 shows the PNS mass found using the fitted relationship in Table 3, including the errors associated with the fitting and the statistical errors associated with the measurement of the total counts or mean energy. The scatter in the simulation points (black) in these plots is indicative of the range of the time for onset of explosion among the different progenitors. Those close to the linear clustering have explosion times <1 s postbounce, while those scattered to higher neutrino count and mean energy values have progressively longer explosion times. Thus, by measuring the number of neutrino counts or mean energy only out to 1 s postbounce, we are probing a smaller and smaller fraction of the total neutrino energy to be released, which in turn is a probe of the gravitational binding energy of the PNS. While we could instead have measured the neutrino emission out to the time of explosion or to the end of the simulation, these are points of time that may be difficult to discern when observing a real

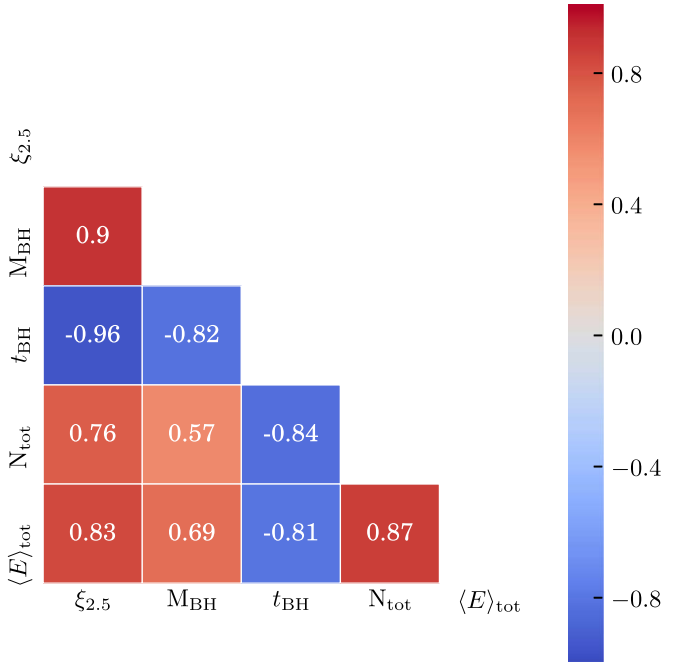

Figure 9. Correlation matrix for observable neutrino quantities and underlying properties of the progenitor and collapse for simulations that do not explode and result in "failed" supernova events, leaving a remnant BH. The quantities considered are core compactness ($\xi_{2.5}$), time to collapse to a BH (t_{BH}), time- and energy-integrated counts in all channels out to 1 s postbounce (N_{tot}), and time-integrated average neutrino energy for all channels ($\langle E\rangle_{tot}$) out to 1 s postbounce. The lower-left half shows the correlation strength, ranging from −1 to 1, as indicated by the color and number in each of the squares.

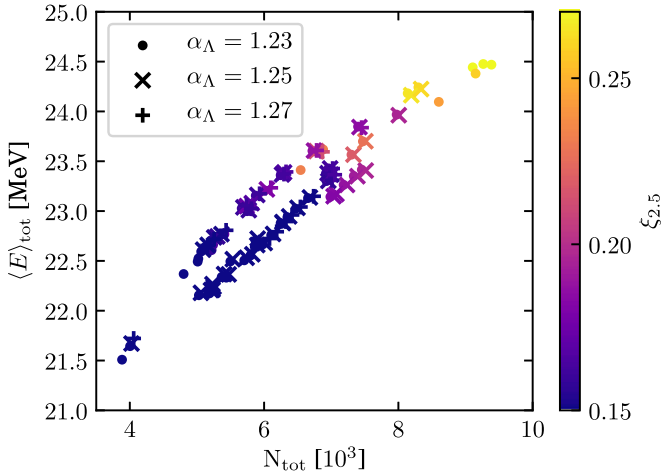

Figure 10. The plane of the neutrino mean energy ($\langle E\rangle_{tot}$) of the time-integrated observed neutrino spectrum vs. time- and energy-integrated counts (N_{tot}) in all channels out to 1 s postbounce, for failed events that collapse to a BH. The color indicates the core compactness of the progenitor star ($\xi_{2.5}$). Symbols indicate the turbulence strength parameter α_Λ used in the simulation. Detections are simulated for a 32 kton water Cerenkov detector for a CCSN event at 10 kpc. Given the lack of scatter with turbulence strength, this measurement appears to be insensitive to the assumptions made in our 1D supernova model.

CCSN event (or in the case of the end of the simulation—a completely arbitrary length of time). Measuring the neutrino counts and average energies lets us compare between simulations using a timescale that can easily be applied to a real CCSN detection.

From Figure 8, it is clear that, at a distance of 10 kpc at least, the error is somewhat reduced when using the number of neutrino counts rather than the mean energy. This is reflected in the larger R^2 value of the fit (0.361 for the mean energy compared to 0.714 for the number of counts) and the strength of the correlations (0.6 for the mean energy compared to 0.85 for the number of counts). Thus, one must take care when considering the fits, such as those shown in Table 3, to also consider what the observational errors may be and use the most beneficial relationship. The fits provided here assume a distance of 10 kpc, so a CCSN event at a farther distance with fewer counts or an event with significant uncertainties in the distance estimation, will not provide as reliable of a determination of the core compactness as indicated by Figure 7, which may make it more precise to use mean energy.

We perform the same analysis for simulations that fail to explode, as is shown in Figure 9. This shows the correlation strength between the observable neutrino quantities; the BH mass, M_{BH}; the core compactness, $\xi_{2.5}$; and the time of collapse to BH, t_{BH}. We consider the time of collapse to a BH an "observable" quantity for the sake of this analysis because it will be easily measurable from the duration of the neutrino emission, from the neutronization burst at bounce to the end of neutrino emission with collapse to a BH. The BH mass was found using the approach of Fernández et al. (2018), which accounts for the unbinding of some of the stellar envelope due to neutrino losses before the collapse to a BH occurs.

Surprisingly though, we find very different relationships between the progenitor properties and neutrino signal for failed supernovae than for successful explosions. In the case of failed explosions, the neutrino mean energy is a better predictor of the core compactness than the neutrino counts. The relationship between the core compactness and time to collapse to a BH evident in Figure 9 has been seen in previous works, first noted by O'Connor & Ott (2011) in studying failed CCSNe in 1D models. The time to collapse to a BH is strongly related to the freefall timescale of the inner 2.5 $M_\odot$ of the progenitor.

Similar to our analysis for the successful explosions, observations of the neutrino count rates and average energies can be used to obtain the core compactness of stars that fail to explode. Figure 10 shows the plane of neutrino average energies and counts for all of our simulations that collapse to a BH, with the core compactness indicated by the color. As with the successful explosions, as shown in Figure 7, these quantities are tightly correlated and show little scatter between different values of the turbulence strength parameter α_Λ. Thus, the progenitor core compactness of a detected failed supernova event could be determined with measurements of the neutrinos out to 1 s postbounce. The coefficients of the linear fit of these data are shown in Table 4, along with a fit for the BH mass. These fits assume the functional form of

$$y = C_{t_{BH}} t_{BH} + C_{N_{tot}} N_{tot} + C_{\langle E\rangle_{tot}} \langle E\rangle_{tot} + D, \quad (5)$$

where t_{BH} is the time postbounce to collapse to a BH, $\langle E\rangle_{tot}$ is the mean energy, and N_{tot} is the number of neutrino counts. We also include the coefficients for a fit that does not include the time to collapse to a BH. Although this fit is not quite as good as that including the time to collapse to a BH, knowing only the neutrino parameters out to 1 s with no knowledge of the collapse time will be sufficient for constraining the core compactness and BH mass.

Table 4
Linear Fit Coefficients for Observable Neutrino Parameters for Failed Supernova Events

Parameter	$C_{t_{\rm BH}}$	$C_{\langle E\rangle_{\rm tot}}$	$C_{N_{\rm tot}}$	D	R^2
$\xi_{2.5}$ (unitless)	$(-3.634 \pm 0.278) \times 10^{-2}$	$(1.572 \pm 0.604) \times 10^{-2}$	⋯	$(-0.412 \pm 1.507) \times 10^{-1}$	0.927
	⋯	$(9.025 \pm 0.336) \times 10^{-2}$	⋯	-1.929 ± 0.0775	0.653
	$(-4.225 \pm 0.322) \times 10^{-2}$	⋯	$(0.000 \pm 3.233\ ) \times 10^{-6}$	$(3.507 \pm 0.338) \times 10^{-1}$	0.918
	⋯	⋯	$(4.409 \pm 0.275) \times 10^{-5}$	$(-1.261 \pm 0.175) \times 10^{-1}$	0.841
$M_{\rm BH}$ ($M_\odot$)	-1.654 ± 0.291	0.356 ± 0.631	⋯	3.545 ± 15.744	0.676
	⋯	3.268 ± 0.465	⋯	-71.084 ± 10.961	0.478
	1.787 ± 0.318	⋯	$(0.000 \pm 3.191) \times 10^{-4}$	$(1.241 \pm 0.333) \times 10^{1}$	0.674
	⋯	⋯	$(1.257 \pm 0.244) \times 10^{-3}$	-3.120 ± 1.773	0.330

Note. Included are fit parameters if time to BH formation is unknown. Coefficients are for a functional fit of the form $y = C_{t_{\rm BH}}\{t_{\rm BH} + C_{N_{\rm tot}}N_{\rm tot} + C_{\langle E\rangle_{\rm tot}}\langle E\rangle_{\rm tot} + D$, with the time to collapse to a BH, $t_{\rm BH}$, measured in seconds and the mean energy, $\langle E\rangle_{\rm tot}$, measured in MeV. R^2 is the correlation coefficient between the data and the fit, and measures the quality of the fit. Note that these fits assume a distance of 10 kpc and thus the number of counts will have to be scaled accordingly for CCSN events at other distances.

It is clear that just 1 s of neutrino detection from the next galactic supernova will provide a wealth of information, and with measurements from a just single detector. Using a network of detectors, with different sensitivities and overall increased count rate, the correlations and constraints shown here should only improve. It is important to note, however, that these results assume an event distance of 10 kpc. For events much farther away with very low count rates, or with significant errors in the distance measurement, the statistical error in the number of counts could become overwhelming and prevent identification of the properties explored here.

Additionally, we do not consider sensitivities to the nuclear equation of state. It is well established that the neutrino emission and the time to collapse to a BH will be sensitive to the equation of state properties (O'Connor & Ott 2011; Schneider et al. 2019; Yasin et al. 2020). Many of these sensitivities, such as those to the symmetry energy and its slope, do not appear in the neutrino emission until many seconds postbounce (Roberts et al. 2012; Schneider et al. 2019) and will not impact the results found here. However, as shown by Schneider et al. (2019), the effective nucleon mass will impact on the neutrino emission in the first second. We leave the exploration of the sensitivity of our parameter estimations to the equation of state to future work.

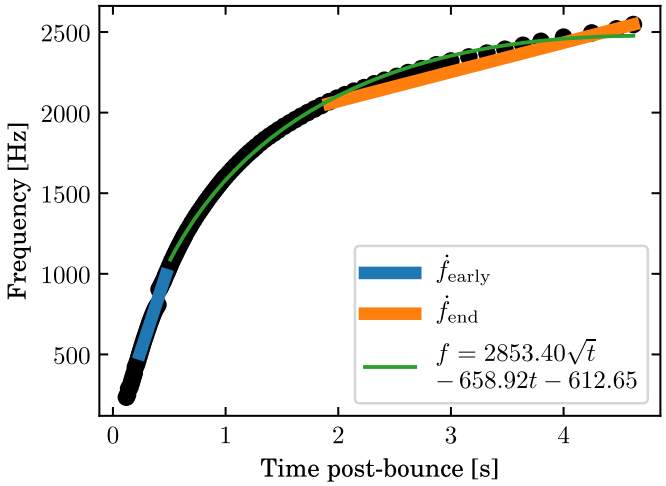

Figure 11. Example of GW quantities considered in the correlation matrix for a 15 $M_\odot$ progenitor with $\alpha_\Lambda = 1.25$, which does not explode successfully. The blue line is the early slope $\dot{f}_{\rm early}$ between 500 and 1000 Hz, and the orange line shows the slope just prior to collapse $\dot{f}_{\rm end}$, between collapse to a BH and 500 Hz below the final frequency. These quantities will be used to compare between simulations and explore correlations with properties of the progenitor and explosion. Green line is the function fit of the peak GW frequency after 0.5 s postbounce.

3.3. GWs

The analysis of the GW emission we perform here provides the peak frequency of the GW emission, but does not provide information about the strength of that emission. Although 2D and 3D simulations provide more detailed and accurate information about the GW emission, it is still beneficial to consider 1D simulations because we can run more 1D simulations (600 in this paper) and can run them to later times than multidimensional simulations.

There have been many previous works that considered the progenitor dependence of the GW emission (Murphy et al. 2009; Müller et al. 2013; Yakunin et al. 2015; Morozova et al. 2018). These works considered the GW signal from 2D simulations of a few progenitor models and largely came to the same conclusions: the peak frequency is not strongly dependent on the progenitor, but the GW energy is much more strongly related to the progenitor. As we will see, we find a similar result here, in that the peak GW frequency is more weakly correlated with the progenitor properties than the neutrino emission, for example, and is not at all correlated with the ZAMS mass. However, many of these studies did not consider the evolution of the peak GW frequency beyond 1 s postbounce. We find that there is little progenitor dependence at early times, but the peak GW frequencies begin to diverge at later times for different progenitors (see, for example, the bottom panel of Figure 4).

In order to quantify the evolution of the dominant GW frequency and easily compare between a large number of simulations, we consider scalar quantities derived from the evolution of the peak frequency: the early slope of the frequency evolution $\dot{f}_{\rm early}$ from 500 to 1000 Hz and additionally, for simulations that result in collapse to a BH, we consider the slope of the frequency just prior to collapse, $\dot{f}_{\rm end}$, from the collapse to a BH to 500 Hz below the frequency at the time of collapse. We chose to use frequencies, rather than times postbounce, as references for defining these slopes as they will be easier to determine from observational data. For nonrotating CCSNe, it will be difficult to determine the time of bounce from the GW signal alone (Pajkos et al. 2019). However, even with current detector resolution, it should be possible to distinguish the time between a 500 Hz frequency

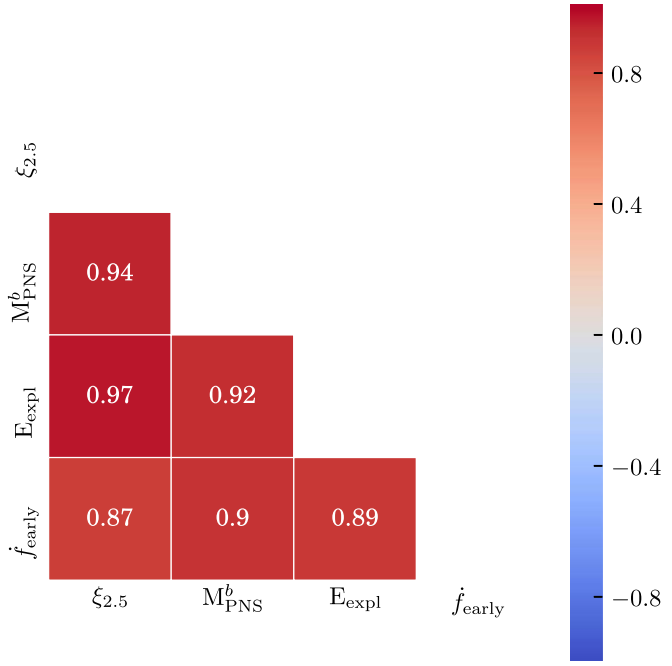

Figure 12. Correlation matrix for observable GW quantities and underlying progenitor and explosion properties for simulations that successfully explode. The quantities considered are core compactness ($\xi_{2.5}$), PNS mass (M^b_{PNS}) at 1 s postbounce, explosion energy (E_{expl}), and early peak GW frequency slope ($\dot{f}_{early}$) between 500 and 1000 Hz. The lower-left half shows the correlation strength, ranging from −1 to 1. Red colors indicate a strong positive correlation and blue a negative correlation, while gray indicates no correlation. The correlation between two values is also indicated by the number in each box.

change. Figure 11 shows an example of the dominant GW frequency evolution from a 1D simulation, for a $15\,M_\odot$ progenitor with $\alpha_\Lambda = 1.25$, as well as the above parameters for this particular simulation. For the same reason, we do not consider the time to collapse to a BH, t_{BH}, to be an "observable" feature from the GW emission alone, because we will not have a reliable indicator of the time of bounce from GWs alone. Additionally, because they are linear, these slopes are not strictly dependent on the specific windows listed here—they could be computed using any available window depending on the available observed data. However, it is worth noting that the end frequency may be difficult to detect as LIGO is not currently very sensitive to frequencies above ∼1000 Hz.

Although the parameters we consider seem rudimentary, we experimented with using various arbitrary functional fits to the frequency evolution with time, but found that as with the neutrino evolution, the fitting parameters were not well correlated with the progenitor and explosion process, especially in comparison with the parameters we have adopted. For example, Morozova et al. (2018) used a quadratic fit of the form $f = At^2 + Bt + C$ to characterize the peak GW frequency between 0.5 and 1.5 s postbounce. However, we have found that although this functional fit captures well the shape of the peak frequency at early times, it fails to capture the behavior as the peak frequency levels out at late times ($t > 1.5$ s postbounce). We propose instead a fit of the form $f = A\sqrt{t} + Bt + C$, which better captures the behavior at later times. An example of such a fit is shown in Figure 11. The coefficients of both functional fits are not well correlated with properties of the progenitor or explosion. Nonetheless, such fits may be useful for studies of detectability, as priors in LIGO

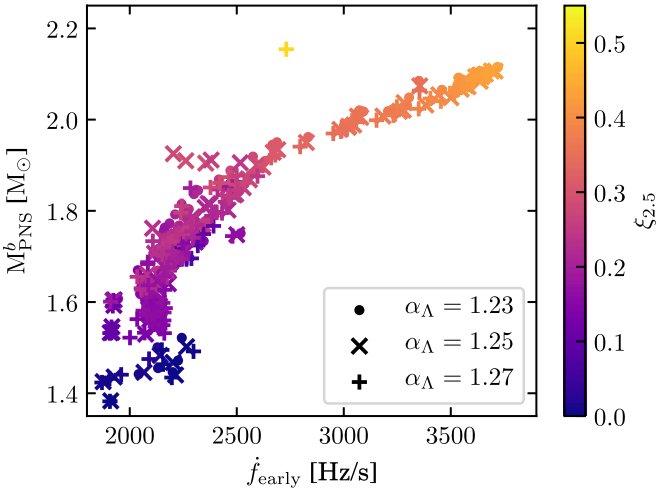

Figure 13. The PNS baryonic mass (M^b_{PNS}) at 1 s postbounce vs. slope of the peak GW frequency ($\dot{f}_{early}$) between 500 and 1000 Hz, for simulations that explode successfully. The core compactness ($\xi_{2.5}$) is indicated by the color. The turbulence strength parameter α_Λ is indicated by the symbol.

data searches, etc., and thus the fit coefficients can be found online,[11] but we will not discuss them further in this work in our exploration of correlated quantities.

It is easiest to see how these GW parameters change with the properties of the progenitor and explosion by looking at the correlation matrix. Figure 12 shows the correlation matrix between progenitor, explosion, and GW properties for simulations that explode successfully. Again, there are many additional parameters that could be included, but all showed weak correlations with the GW emission and thus we do not include them here. The GW eigenfrequencies are intimately related to the PNS mass and the core compactness $\xi_{2.5}$, because they are sensitive to the structure of the core and its evolution.

The PNS mass, M^b_{PNS}, at 1 s postbounce is strongly correlated with the early-time evolution of the dominant GW frequency $\dot{f}_{early}$. Thus, similar to what we have done with the neutrino emission, the PNS mass can be constrained by the GW emission. Figure 13 shows the PNS mass versus the early-time evolution of the peak GW frequency ($\dot{f}_{early}$). The trend here is less clear than for the neutrino counts, which is to be expected given the weaker correlations between the GW emission and PNS mass than for the neutrino counts. Nonetheless, detection of the early GW signal will again provide an independent measure of the PNS mass before fallback occurs. Table 5 contains the linear fit coefficients for these parameters and the core compactness, PNS mass, and explosion energy. These fits use the functional form

$$y = C_{\dot{f}_{early}} \dot{f}_{early} + D, \tag{6}$$

where $\dot{f}_{early}$ is the early-time evolution of the peak GW frequency. Note that there is clearly a nonlinear relationship between these variables, and a nonlinear fit may provide a stronger correlation and fit estimation.

Similarly, we can consider the relationship between progenitor and GW properties for failed explosions, as shown in Figure 14. We consider the core compactness $\xi_{2.5}$ and BH mass M_{BH}. Again, we do not consider the time to collapse to a BH an "observable" quantity, for the sake of this analysis, as it will not be easily measurable from the duration of the

[11] Publicly available at [doi:10.5281/zenodo.3822555].

Table 5
Linear Fit Coefficients for Observable GW Parameters for Successful Supernova Events for the Core Compactness ($\xi_{2.5}$), Baryonic PNS Mass at 1 s Postbounce ($M^b_{\rm PNS}$), and Explosion Energy ($E_{\rm expl}$)

Parameter	$C_{\dot{f}_{\rm early}}$	D	R^2
$\xi_{2.5}$ (unitless)	$(1.790 \pm 0.047) \times 10^{-4}$	$(-2.110 \pm 0.118) \times 10^{-1}$	0.763
$M^b_{\rm PNS}$ ($M_\odot$)	$(3.131 \pm 0.070) \times 10^{-4}$	$(9.945 \pm 0.175) \times 10^{-1}$	0.818
$E_{\rm expl}$ (10^{51} erg)	$(6.848 \pm 0.169) \times 10^{-4}$	$(-7.880 \pm 0.427) \times 10^{-1}$	0.784

Note. Coefficients are for functional fits of the form $y = C_{\dot{f}_{\rm early}} \dot{f}_{\rm early} + D$, with $\dot{f}_{\rm early}$ measured in Hz s^{-1}. R^2 is the correlation coefficient between the data and the fit, and measures the quality of the fit.

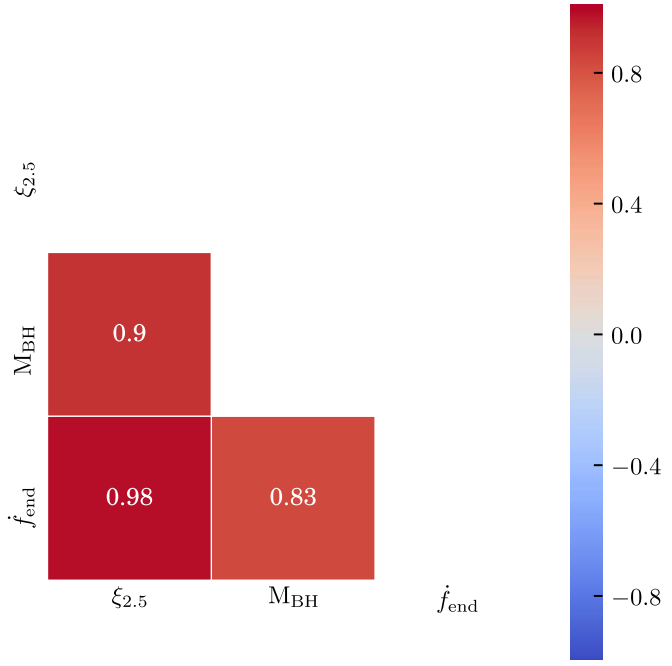

Figure 14. Correlation matrix for observable GW quantities and underlying progenitor for simulations that do not explode and result in "failed" supernova events. The quantities considered are core compactness ($\xi_{2.5}$), BH mass ($M_{\rm BH}$), and late GW frequency slope ($\dot{f}_{\rm end}$) just prior to collapse to BH. The lower-left half shows the correlation strength, ranging from −1 to 1.

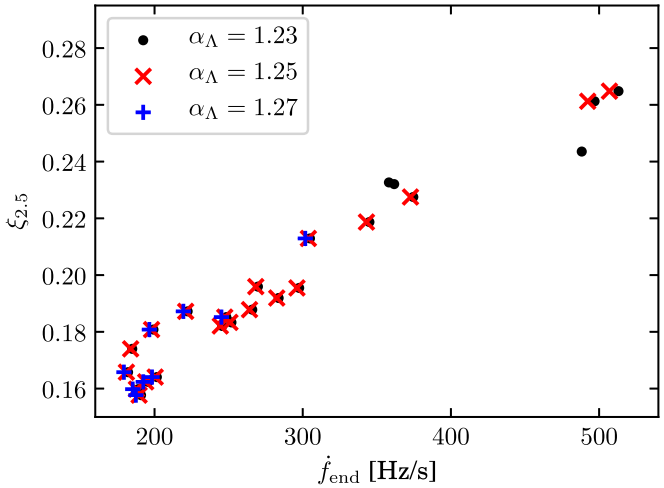

Figure 15. Core compactness, $\xi_{2.5}$, vs. the slope of the late-time dominant GW frequency, $\dot{f}_{\rm end}$, for simulations that fail to explode. The turbulence strength parameter α_Λ is indicated by the color and symbol.

GW emission. A tight connectio between the core compactness and BH formation time was pointed out by O'Connor & Ott (2011), who connected the BH formation time with the freefall timescale of the 2.5 $M_\odot$ mass shell. It may be possible to discern the BH formation time indirectly from the compactness.

Surprisingly, or perhaps unsurprisingly after our discussion of the neutrino emission, there is a stronger relationship between the core compactness $\xi_{2.5}$ and the GW emission here than for successful explosions. The late-time evolution of the dominant frequency $\dot{f}_{\rm end}$ just prior to collapse to a BH correlates strongly with the core compactness. Figure 15 shows the core compactness versus the evolution of the dominant GW frequency just prior to collapse to a BH. There is a clear, distinct trend in core compactness and GW emission. Table 6 provides the fits between the observable GW emission and the core compactness and BH mass for core-collapse events that fail to explode, assuming a function of the form

$$y = C_{\dot{f}_{\rm end}} \dot{f}_{\rm end} + D, \quad (7)$$

where $\dot{f}_{\rm end}$ is the late-time evolution of the dominant GW frequency.

In summary, the GW emission provides an additional window into the central engine of CCSNe. With detections of only the dominant GW frequency, we will be able to place tight constraints on the progenitor star and remnant compact object. We only consider the GW emission from eigenmodes of the PNS and not from the convective material near the shock, which may encode additional information about the progenitor (Torres-Forné et al. 2019a).

3.4. Combined Analysis

We have shown that detection of either neutrinos or GWs from a nearby CCSN will provide constraints on the stellar structure, mass of the PNS and BH prior to fallback, and explosion energy. However, it is likely that we will have detections of both GWs and neutrinos from such an event. For successful and failed explosions, neutrino and GW quantities are both strongly correlated with the same properties of the progenitor and explosion. Therefore, combining these detections may provide an even more robust way to constrain the progenitor and explosion properties of interest.

For successful explosions, both the neutrino counts and GW evolution are correlated with the core compactness, $\xi_{2.5}$; PNS mass at 1 s postbounce, $M^b_{\rm PNS}$; and explosion energy $E_{\rm expl}$, as shown in Figure 6 and 12. Table 7 contains the linear fit coefficients for a combined measurement using both neutrinos

Table 6
Linear Fit Coefficients for Observable GW Parameters from Failed Supernova Events for the Core Compactness ($\xi_{2.5}$) and BH Mass ($M_{\rm BH}$)

Parameter	$C_{\dot{f}_{\rm end}}$	D	R^2
$\xi_{2.5}$ (unitless)	$(2.873 \pm 0.083) \times 10^{-4}$	$(1.143 \pm 0.027) \times 10^{-1}$	0.957
$M_{\rm BH}$ ($M_\odot$)	$(1.208 \pm 0.109) \times 10^{-2}$	2.428 ± 0.347	0.694

Note. Coefficients are for functional fit of the form $y = C_{\dot{f}_{\rm end}}\dot{f}_{\rm end} + D$, with $\dot{f}_{\rm end}$ measured in Hz s^{-1}. R^2 is the correlation coefficient between the data and the fit, and measures the quality of the fit.

Table 7
Linear Fit Coefficients to Observable Neutrino and GW Parameters for Successfully Exploding CCSN Events for the Core Compactness ($\xi_{2.5}$), PNS Mass at 1 s Postbounce ($M^b_{\rm PNS}$), and Explosion Energy ($E_{\rm expl}$)

Parameter	$C_{N_{\rm tot}}$	$C_{\langle E\rangle_{\rm tot}}$	$C_{\dot{f}_{\rm early}}$	D	R^2
$\xi_{2.5}$ (unitless)	$(3.771 \pm 0.409) \times 10^{-5}$	⋯	$(1.130 \pm 0.083) \times 10^{-4}$	$(-2.034 \pm 0.109) \times 10^{-1}$	0.801
	⋯	$(1.926 \pm 0.487) \times 10^{-2}$	$(1.637 \pm 0.060) \times 10^{-4}$	$(-5.690 \pm 0.912) \times 10^{-1}$	0.771
$M^b_{\rm PNS}$ ($M_\odot$)	$(1.152 \pm 0.038) \times 10^{-4}$	⋯	$(1.126 \pm 0.076) \times 10^{-4}$	1.018 ± 0.010	0.941
	⋯	$(9.634 \pm 0.058) \times 10^{-2}$	$(2.388 \pm 0.070) \times 10^{-4}$	$(-7.959 \pm 1.079) \times 10^{-1}$	0.888
$E_{\rm expl}$ (10^{51} erg)	$(1.291 \pm 0.149) \times 10^{-4}$	⋯	$(4.600 \pm 0.303) \times 10^{-4}$	$(-7.620 \pm 0.397) \times 10^{-1}$	0.815
	⋯	$(7.161 \pm 1.754) \times 10^{-2}$	$(6.295 \pm 0.215) \times 10^{-4}$	-2.119 ± 0.329	0.792

Note. Coefficients are for functional fit of the form $y = C_{N_{\rm tot}}N_{\rm tot} + C_{\langle E\rangle_{\rm tot}}\langle E\rangle_{\rm tot} + C_{\dot{f}_{\rm early}}\dot{f}_{\rm early} + D$, with the mean energy, $\langle E\rangle_{\rm tot}$, measured in MeV and $\dot{f}_{\rm early}$ measured in Hz s^{-1}. R^2 is the correlation coefficient between the data and the fit, and measures the quality of the fit. Note that these fits assume a distance of 10 kpc and thus the number of counts will have to be scaled accordingly for CCSN events at other distances.

Table 8
Linear Fit Coefficients to Observable Neutrino and GW Parameters for Failed Supernova Events for the Core Compactness ($\xi_{2.5}$) and BH Mass ($M_{\rm BH}$)

Parameter	$C_{t_{\rm BH}}$	$C_{\dot{f}_{\rm end}}$	D	R^2
$\xi_{2.5}$ (unitless)	$(-1.074 \pm 0.429) \times 10^{-2}$	$(2.186 \pm 0.286) \times 10^{-4}$	$(1.732 \pm 0.236) \times 10^{-1}$	0.961
	⋯	$(2.873 \pm 0.083) \times 10^{-4}$	$(1.114 \pm 0.026) \times 10^{-1}$	0.957
$M_{\rm BH}$ ($M_\odot$)	$(-5.837 \pm 5.894) \times 10^{-1}$	$(8.348 \pm 3.927) \times 10^{-3}$	5.626 ± 3.248	0.700
	⋯	$(1.208 \pm 0.109) \times 10^{-2}$	2.428 ± 0.347	0.694

Note. Included are fit parameters if time to BH formation is unknown. Coefficients are for functional fits of the form $y = C_{t_{\rm BH}}t_{\rm BH} + C_{\dot{f}_{\rm end}}\dot{f}_{\rm end} + D$, with the time to collapse to BH, $t_{\rm BH}$, measured in seconds, and $\dot{f}_{\rm end}$ measured in Hz s^{-1}. R^2 is the correlation coefficient between the data and the fit, and measures the quality of the fit. Note that these fits assume a distance of 10 kpc and thus the number of counts will have to be scaled accordingly for CCSN events at other distances.

and GWs, using a function of the form

$$y = C_{N_{\rm tot}}N_{\rm tot} + C_{\langle E\rangle_{\rm tot}}\langle E\rangle_{\rm tot} + C_{\dot{f}_{\rm early}}\dot{f}_{\rm early} + D, \quad (8)$$

where $N_{\rm tot}$ is the number of neutrino counts, $\langle E\rangle_{\rm tot}$ is the neutrino mean energy, and $\dot{f}_{\rm early}$ is the early-time evolution of the dominant GW frequency. By simultaneously using neutrino and GW information, there is an improvement in the quality of the fit, as measured by the R^2, for both the core compactness and PNS mass. For example, the R^2 of the fit for the core compactness was 0.841 using just the neutrino counts and 0.763 using the GW slope, but is increased to 0.801 when using both neutrino counts and the GW information. The addition of GW information to the neutrino information may prove to be an invaluable addition to constraining the core compactness, PNS mass, and explosion energy for CCSN events at large distances with low count rates or for events with large uncertainties on the distance.

For failed supernova events, both the neutrino and GW observables are correlated with the core compactness, $\xi_{2.5}$, and remnant BH mass, $M_{\rm BH}$. For both of these parameters, the quality of the fit is not noticeably improved by combining observables from both messengers. Table 8 contains the fit coefficients for such a combined analysis, using a function of the form

$$y = C_{t_{\rm BH}}t_{\rm BH} + C_{\dot{f}_{\rm end}}\dot{f}_{\rm end} + D, \quad (9)$$

where $t_{\rm BH}$ is the time to BH formation and $\dot{f}_{\rm end}$ is the late-time evolution of the dominant GW frequency. Including the neutrino mean energy $\langle E\rangle_{\rm tot}$ or total counts $N_{\rm tot}$ along with the GW information was not advantageous and overconstrained the fit, leading to the coefficients on the neutrino data to be zero in the fit. These fits are not included here. There is a slight improvement in the quality of the fit if the time to BH formation, $t_{\rm BH}$, as could be measured using neutrinos, is included alongside the slope of the GW frequency $\dot{f}_{\rm end}$. For the core compactness, the R^2 value increases to 0.961 from 0.957 if the time to BH formation is included in the fit. For failed CCSN events, it will perhaps be more significant to determine the core compactness and BH mass from the neutrino and GW signals separately, because they both independently provide tight constraints on these parameters and ensure that they are in agreement. Disagreement in core compactness and/or BH mass as determined from the GW and neutrino signals separately

would be indicative that we do not fully understand the neutrino and GW emission from failed CCSNe.

4. Discussion and Conclusions

Using 600 one-dimensional simulations of CCSNe from 9 to 120 $M_{\odot}$, carried out with the STIR model in the FLASH supernova code, we analyze the observable neutrino and GW signals to study the correlations with properties of the progenitor star, explosion mechanism, and remnant compact object. To model the neutrinos, we simulate the detected neutrino signal in a 32 kton Super Kamiokande–like water Cerenkov detector using the SNOwGLoBES code. To model the GWs, we conduct an astroseismology analysis of the PNS structure to determine the dominant GW frequency.

Given the significant computational expense of 3D simulations, it is not currently feasible to use 3D simulations to make predictions of the multimessenger signals of the entire range of possible CCSN events. One-dimensional simulations remain vital for performing parameter and population studies such as this. Although these simulations are done in 1D, they have been shown to reproduce the features of 3D simulations. The STIR model uses a Reynolds-averaged decomposition of the Euler equations to model the effects of turbulence in 1D simulations and reproduces the behavior of 3D simulations (Couch et al. 2020). Additionally, the GW eigenfrequencies found here match the peak GW frequency seen in 3D simulations, as shown in Figure 3.

To address the questions posed in the introduction: first, will we be able to distinguish between a "successful" versus "failed" CCSN event without direct detection of EM emission? We find that, with measurement of the first few seconds of neutrino and GW emission from a nearby CCSN, we may be able to determine whether or not it will explode successfully before observing EM emission. The time of collapse to a BH in failed CCSNe will be marked by a sharp end in both neutrino and GW emission. More significantly, it may be possible to determine the time that the explosion sets in from a drop in both the neutrino counts and mean energy, but with continued emission at a lower rate and mean energy, as shown in Figure 4. The drop in the neutrino count rate and mean energy is tied to the decrease in the mass accretion onto the PNS after explosion sets in, an effect that is significantly enhanced in 1D compared to multidimensional simulations. The same effect is visible in current multidimensional simulations, although less pronounced.

Second, what can we tell about the progenitor star, explosion mechanism, and remnant compact object from detection of neutrinos, GWs, or both? Additional quantitative information about the progenitor and explosion can also be determined from just a few seconds of detection as well, such as a determination of the PNS and BH mass and core compactness. The neutrino and GW emission are strongly correlated with these parameters. Determining these quantities from the neutrino and GW emission will aid in placing constraints on the progenitor star, independent of preexplosion imaging, the evolution of the compact object prior to fallback accretion, and the explosion energy, independent of the light curve. If we can determine the core compactness of the next galactic CCSN with neutrino and GW emission, we can then compare that quantity with the results of stellar evolution calculations and the stellar mass found from preexplosion imaging to either validate or constrain current stellar evolution models. We provide fits to our simulations that connect the observable neutrino and GW parameters with the core compactness, explosion energy, PNS mass, and remnant BH mass. Additionally, we are making the neutrino and GW emission from our simulations publicly available, in hopes that they can be used in future studies of detectability and optimization of detector signal processing.

Although previous works have claimed that there is little progenitor dependence in the GW signal (Murphy et al. 2009; Müller et al. 2013; Yakunin et al. 2015; Morozova et al. 2018), we have found that the evolution of the GW signal is strongly correlated with the core compactness, remnant compact object mass, and explosion energy; for example, the core compactness and BH mass are tightly correlated with the dominant GW frequency for massive stars that do not explode, as shown in Figure 14. Although there are significant differences between progenitors in the overall magnitude of the peak GW frequency at a given time postbounce (for example, see the bottom panel of Figure 4), we have limited ourselves to considering the slope of the GW signal. These differences in the overall magnitude should be well described by the differences in the early slope of the peak GW frequency, which we have explored here. More work must be done to determine how well this result holds up in multidimensional simulations, as well as after considering proper detector response. Multidimensional effects, such as accretion, rotation, and SASI, may impact the late-time GW emission in ways that cannot be captured in spherically symmetric simulations. Additionally, there will be significant information embedded in the strength of the GW signal, as well, which cannot be explored using 1D.

The correlations and fits found here assume an event distance of 10 kpc. Thus, for the fits provided, the number of neutrino counts must be scaled appropriately for events at different distances. We find that, at 10 kpc, the errors on the number of counts will be small and allow for a reliable determination of parameters such as the PNS mass, as shown in Figure 7. However, for events at larger distances where the count rate is low, or if there is a large error associated with the distance determination, the number of neutrino counts (scaled to 10 kpc for use in our fits) may have a larger error and make it preferable to use the mean energy or GW emission in the determination of the core compactness and other parameters. We consider only the neutrino detections in a single neutrino detector—Super Kamiokande. The next galactic supernova will be detected in a multitude of detectors, all providing additional insight and information on the CCSN environment. The different detector sensitivities and overall increased count rates will only increase the significance of the correlations and relationships found here and may provide new correlations and insights.

We find that, for successful CCSN events, combining the neutrino and GW information will improve the determination of parameters such as the core compactness. However, for failed CCSN events, combining the neutrino and GW information did not improve the quality of fit in the determining the core compactness or BH mass. Both signals will independently be able to constrain these quantities quite well, though, and combining them in this case may be artificially overconstraining the fit. Even if both neutrinos and GWs are not detected, we see that the measurement of just one "messenger" will still provide constraints on the stellar structure and remnant compact object. It is promising that, for the next nearby CCSN event, there are multiple avenues for using either the GW or neutrino emission, or both, to constrain the stellar structure and remnant compact object and doing so does not depend on getting a single, specific detection with high precision.

Similarly, we only consider the evolution of the dominant GW frequency. There will be detections of GW emission in other frequency bands, which also contain information about the structure of the PNS, and the convection and turbulence occurring above it that excite those modes. Further work must be done to determine what other frequency bands may be detectable with current and near-future detector sensitivities and what information they encode about the CCSN environment. Additionally, we take care with the neutrino emission to explore only detectable features by using SNOwGLoBES to simulate a realistic detected signal, but no such code is publicly available to simulate the detector response and reconstruction for GW signals. Hopefully, by focusing on the peak GW frequency and its slope over broad spans of time, we have chosen detectable features.

The framework for the analysis of CCSN simulations presented here has many possible applications and avenues for expansion. There is already a significant body of work that explores the relationship between the supernova light curve and explosion energy, nucleosynthesis, etc. The approach taken in this work can be applied to studies of the light curve as well and may aid in uncovering connections between EM detections, other multimessenger signals, and progenitor properties (B. Barker et al. 2019a, in preparation). As we see here, combining information from different sources can prove to be more insightful than a single source alone. Including EM emission in our correlation analysis may uncover connections between the core of the event, as detected in neutrinos and GWs, and the shock propagation and explosion, as detected in EM emission. Additionally, there has been no systematic study of EM emission from failed supernovae (Lovegrove & Woosley 2013; Quataert et al. 2019). Correlations between EM emission and other signals may prove to be just as significant for failed events as for successful explosions.

We limit ourselves to linear correlations between the properties in this work. There are far more complex and interesting relationships between the progenitor, CCSN environment, and detectable quantities than can be fully captured by linear relationships. It is, if anything, quite shocking how strong the linear correlations are. Future work will loosen this constraint by considering nonlinear correlations and more complex functional fits between observable quantities and progenitor and explosion properties.

Finally, there is significant and impactful physics that has not been considered here. Uncertainties due to binarity, rotation, and equation of state will add uncertainty to the determination of progenitor and explosion properties from multimessenger signals. However, these properties of rotation, equation of state, etc., may also have their own strong correlations with information encoded in the GW and neutrino signals. For example, Westernacher-Schneider et al. (2019) found a relationship between the rotation and GW and neutrino emission that may be encoded in correlations such as those explored here. Schneider et al. (2019) found correlations between equation of state parameters and neutrino emission in a $20\,M_{\odot}$ progenitor, and Richers et al. (2017) explored correlations between equation of state parameters and the GW signal at bounce for rotating CCSNe. Thus, multimessenger detections may be able to provide constraints on additional stellar properties not considered in this work, and perhaps could be used to place constraints on other aspects of the problem such as the nuclear equation of state. We plan to explore the sensitivity of the correlations found in this work to the nuclear equation of state, and any possible correlations between multimessenger signals and equation of state parameters, in future work (B. Barker et al. 2019b, in preparation).

Perhaps the most significant omission is that of neutrino flavor mixing. We fundamentally do not know what flavor mixing processes may occur in CCSNe, and under what conditions. Flavor mixing processes such as collective oscillations (Duan et al. 2010) and fast oscillations (Sawyer 2005, 2009; Johns et al. 2020; Martin et al. 2020; Morinaga et al. 2020) have only been studied using stability analysis or simplified conditions. The occurrence of any of these processes in the CCSN environment would drastically change how the observed neutrino signal is related to the GW emission, progenitor properties, and explosion dynamics. It is worth noting, however, that the information contained in the neutrino signal may not be "lost" if significant flavor mixing processes occur—merely, in some sense, scrambled.

There is a wealth of information that will be embedded in the neutrino and GW emission of the next nearby CCSN event and, with modern neutrino and GW detectors, we are well prepared to make such a detection. However, interpreting these observations will require understanding the emission from all possible CCSN events, spanning the range of progenitor mass, metallicity, rotation, etc., and understanding the impact of the nuclear equation of state and other fundamental physics uncertainties. Given the computational cost of 3D simulations, we must continue to rely on 1D simulations to understand the span of possible CCSNe for the foreseeable future. The study we conduct here is a first step in the process of predicting multimessenger signals from all possible CCSNe and developing a framework to interpret the large number of simulations required to understand the landscape of CCSN events.

The authors would like to thank Kate Scholberg, Gail Mclaughlin, and Jim Kneller for insightful conversations about this work and Jost Migenda for helping with the formatting of the publicly available neutrino fluxes. M.L.W. is supported by an NSF Astronomy and Astrophysics Postdoctoral Fellowship under award AST-1801844 and by the U. S. Department of Energy, Office of Science, Office of Nuclear Physics, under award number DE-SC0015904. S.M.C. is supported by the U. S. Department of Energy, Office of Science, Office of Nuclear Physics, under award numbers DE-SC0015904 and DE-SC0017955. E.O. is supported by the Swedish Research Council under award number 2018-04575. This work was supported in part by Michigan State University through computational resources provided by the Institute for Cyber-Enabled Research.

Software: FLASH (Fryxell et al. 2000; Dubey et al. 2009), SNOwGLoBES (Scholberg 2012), astroseismology analysis code (Morozova et al. 2018), Matplotlib (Hunter 2007), Numpy (van der Walt et al. 2011), SciPy (Jones et al. 2001), NuLib (O'Connor 2015).

ORCID iDs

MacKenzie L. Warren https://orcid.org/0000-0001-9440-6017
Sean M. Couch https://orcid.org/0000-0002-5080-5996
Evan P. O'Connor https://orcid.org/0000-0002-8228-796X
Viktoriya Morozova https://orcid.org/0000-0002-0674-5930

References

Abbott, B. P., Abbott, R., Abbott, T. D., et al. 2016, PhRvD, 94, 102001
Adams, S. M., Kochanek, C. S., Gerke, J. R., & Stanek, K. Z. 2017, MNRAS, 469, 1445

Andresen, H., Müller, E., Janka, H. T., et al. 2019, MNRAS, 486, 2238
Arnett, W. D., Bahcall, J. N., Kirshner, R. P., & Woosley, S. E. 1989, ARA&A, 27, 629
Baron, E., & Cooperstein, J. 1990, ApJ, 353, 597
Bethe, H. A. 1990, RvMP, 62, 801
Borriello, E., Chakraborty, S., Mirizzi, A., Serpico, P. D., & Tamborra, I. 2012, PhRvD, 86, 083004
Bruenn, S. W. 1985, ApJS, 58, 771
Buonanno, A., Sigl, G., Raffelt, G. G., Janka, H.-T., & Müller, E. 2005, PhRvD, 72, 084001
Burrows, A. 2013, RvMP, 85, 245
Burrows, A., Radice, D., & Vartanyan, D. 2019, MNRAS, 485, 3153
Cabezón, R. M., Pan, K.-C., Liebendörfer, M., et al. 2018, A&A, 619, A118
Camelio, G., Lovato, A., Gualtieri, L., et al. 2017, PhRvD, 96, 043015
Cardall, C. Y., Endeve, E., & Mezzacappa, A. 2013, PhRvD, 87, 103004
Clausen, D., Piro, A. L., & Ott, C. D. 2015, ApJ, 799, 190
Couch, S. M. 2017, RSPTA, 375, 20160271
Couch, S. M., & Ott, C. D. 2015, ApJ, 799, 5
Couch, S. M., Warren, M. L., & O'Connor, E. P. 2020, ApJ, 890, 127
Cox, J. P., & Giuli, R. T. 1968, Principles of Stellar Structure (Cambridge: Cambridge Scientific Publishers)
Crocker, K., Prestegard, T., Mandic, V., et al. 2017, PhRvD, 95, 063015
Dighe, A. S., & Smirnov, A. Y. 2000, PhRvD, 62, 033007
Duan, H., Fuller, G., & Qian, Y. 2010, ARNPS, 60, 569
Dubey, A., Antypas, K., Ganapathy, M. K., et al. 2009, ParC, 35, 512
Ebinger, K., Curtis, S., Fröhlich, C., et al. 2019, ApJ, 870, 1
Ertl, T., Janka, H.-T., Woosley, S. E., Sukhbold, T., & Ugliano, M. 2016, ApJ, 818, 124
Farmer, R., Fields, C. E., Petermann, I., et al. 2016, ApJS, 227, 22
Farrell, E. J., Groh, J. H., Meynet, G., & Eldridge, J. J. 2020, MNRAS, 494, L53
Fernández, R., Quataert, E., Kashiyama, K., & Coughlin, E. R. 2018, MNRAS, 476, 2366
Fröhlich, C., Hauser, P., Liebendörfer, M., et al. 2006a, ApJ, 637, 415
Fröhlich, C., Hix, W. R., Martínez-Pinedo, G., et al. 2006b, NewAR, 50, 496
Fröhlich, C., Martínez-Pinedo, G., Liebendörfer, M., et al. 2006c, PhRvL, 96, 142502
Fryer, C. L. 1999, ApJ, 522, 413
Fryxell, B., Olson, K., Ricker, P., et al. 2000, ApJS, 131, 273
Fuller, J., Klion, H., Abdikamalov, E., & Ott, C. D. 2015, MNRAS, 450, 414
Hidaka, J., Kajino, T., & Mathews, G. J. 2018, ApJ, 869, 31
Himmel, A., & Scholberg, K. 2016, NPPP, 273, 1897
Horiuchi, S., & Kneller, J. P. 2018, JPhG, 45, 043002
Horiuchi, S., Nakamura, K., Takiwaki, T., & Kotake, K. 2017, JPhG, 44, 114001
Horowitz, C. J. 2002, PhRvD, 65, 043001
Hunter, J. D. 2007, CSE, 9, 90
Hyper-Kamiokande Proto-Collaboration, Abe, K., Ade, K., et al. 2018, PTEP, 2018, 063C01
Janka, H.-T. 2012, ARNPS, 62, 407
Janka, H.-T., Hanke, F., Hüdepohl, L., et al. 2012, PTEP, 2012, 01A309
Janka, H.-T., Langanke, K., Marek, A., Martínez-Pinedo, G., & Müller, B. 2007, PhR, 442, 38
Janka, H.-T., Melson, T., & Summa, A. 2016, ARNPS, 66, 341
Johns, L., Nagakura, H., Fuller, G. M., & Burrows, A. 2020, PhRvD, 101, 043009
Jones, E., Oliphant, T., Peterson, P., et al. 2001, SciPy: Open Source Scientific Tools for Python, http://www.scipy.org/
Keil, M. T., Raffelt, G. G., & Janka, H.-T. 2003, ApJ, 590, 971
Kotake, K., Ohnishi, N., & Yamada, S. 2007, ApJ, 655, 406
Kuroda, T., Kotake, K., Hayama, K., & Takiwaki, T. 2017, ApJ, 851, 62
Kuroda, T., Kotake, K., & Takiwaki, T. 2016, ApJL, 829, L14
Lentz, E. J., Bruenn, S. W., Hix, W. R., et al. 2015, ApJL, 807, L31
Liebendörfer, M., Messer, O. E. B., Mezzacappa, A., et al. 2004, ApJS, 150, 263
Lovegrove, E., & Woosley, S. E. 2013, ApJ, 769, 109
Mabanta, Q. A., & Murphy, J. W. 2018, ApJ, 856, 22
Mabanta, Q. A., Murphy, J. W., & Dolence, J. C. 2019, ApJ, 887, 43
Marek, A., Janka, H.-T., & Müller, E. 2009, A&A, 496, 475
Martin, J. D., Yi, C., & Duan, H. 2020, PhLB, 800, 135088
Mathews, G. J., Boccioli, L., Hidaka, J., & Kajino, T. 2019, arXiv:1907.10088
Melson, T., Janka, H.-T., & Marek, A. 2015, ApJL, 801, L24
Møller, K., Suliga, A. M., Tamborra, I., & Denton, P. B. 2018, JCAP, 2018, 066
Morinaga, T., Nagakura, H., Kato, C., & Yamada, S. 2020, PhRvR, 2, 012046
Morozova, V., Radice, D., Burrows, A., & Vartanyan, D. 2018, ApJ, 861, 10
Müller, B. 2016, PASA, 33, e048
Müller, B. 2019, MNRAS, 487, 5304
Müller, B., Heger, A., Liptai, D., & Cameron, J. B. 2016, MNRAS, 460, 742
Müller, B., Janka, H.-T., & Marek, A. 2013, ApJ, 766, 43
Müller, B., Tauris, T. M., Heger, A., et al. 2019, MNRAS, 484, 3307
Murphy, J. W., & Burrows, A. 2008, ApJ, 688, 1159
Murphy, J. W., Dolence, J. C., & Burrows, A. 2013, ApJ, 771, 52
Murphy, J. W., & Meakin, C. 2011, ApJ, 742, 74
Murphy, J. W., Ott, C. D., & Burrows, A. 2009, ApJ, 707, 1173
Nagakura, H., Burrows, A., Radice, D., & Vartanyan, D. 2019, MNRAS, 490, 4622
Nakamura, K., Takiwaki, T., Kuroda, T., & Kotake, K. 2015, PASJ, 67, 107
O'Connor, E. 2015, ApJS, 219, 24
O'Connor, E., & Ott, C. D. 2011, ApJ, 730, 70
O'Connor, E., & Ott, C. D. 2013, ApJ, 762, 126
O'Connor, E. P., & Couch, S. M. 2018a, ApJ, 854, 63
O'Connor, E. P., & Couch, S. M. 2018b, ApJ, 865, 81
Ott, C. D., Roberts, L. F., da Silva Schneider, A., et al. 2018, ApJ, 855, L3
Pajkos, M. A., Couch, S. M., Pan, K.-C., & O'Connor, E. P. 2019, ApJ, 878, 13
Pan, K.-C., Liebendörfer, M., Couch, S. M., & Thielemann, F.-K. 2018, ApJ, 857, 13
Paxton, B., Bildsten, L., Dotter, A., et al. 2011, ApJS, 192, 3
Paxton, B., Cantiello, M., Arras, P., et al. 2013, ApJS, 208, 4
Paxton, B., Marchant, P., Schwab, J., et al. 2015, ApJS, 220, 15
Pejcha, O., & Thompson, T. A. 2015, ApJ, 801, 90
Perego, A., Hempel, M., Fröhlich, C., et al. 2015, ApJ, 806, 275
Quataert, E., Lecoanet, D., & Coughlin, E. R. 2019, MNRAS, 485, L83
Radice, D., Bernuzzi, S., Del Pozzo, W., Roberts, L. F., & Ott, C. D. 2017, ApJL, 842, L10
Radice, D., Morozova, V., Burrows, A., Vartanyan, D., & Nagakura, H. 2019, ApJL, 876, L9
Richers, S., Ott, C. D., Abdikamalov, E., O'Connor, E., & Sullivan, C. 2017, PhRvD, 95, 063019
Roberts, L. F., Shen, G., Cirigliano, V., et al. 2012, PhRvL, 108, 061103
Sawyer, R. F. 2005, PhRvD, 72, 045003
Sawyer, R. F. 2009, PhRvD, 79, 105003
Schneider, A. S., Roberts, L. F., Ott, C. D., & O'Connor, E. 2019, PhRvC, 100, 055802
Scholberg, K. 2012, ARNPS, 62, 81
Seadrow, S., Burrows, A., Vartanyan, D., Radice, D., & Skinner, M. A. 2018, MNRAS, 480, 4710
Shibata, M., Kiuchi, K., Sekiguchi, Y., & Suwa, Y. 2011, PThPh, 125, 1255
Shu, C.-W., & Osher, S. 1988, JCoPh, 77, 439
Smartt, S. J. 2009, ARA&A, 47, 63
Sotani, H., Kuroda, T., Takiwaki, T., & Kotake, K. 2017, PhRvD, 96, 063005
Sotani, H., Kuroda, T., Takiwaki, T., & Kotake, K. 2019, PhRvD, 99, 123024
Sotani, H., & Sumiyoshi, K. 2019, PhRvD, 100, 083008
Sotani, H., & Takiwaki, T. 2016, PhRvD, 94, 044043
Steiner, A. W., Hempel, M., & Fischer, T. 2013, ApJ, 774, 17
Sukhbold, T., & Adams, S. 2020, MNRAS, 492, 2578
Sukhbold, T., Ertl, T., Woosley, S. E., Brown, J. M., & Janka, H.-T. 2016, ApJ, 821, 38
Sukhbold, T., Woosley, S. E., & Heger, A. 2018, ApJ, 860, 93
Sumiyoshi, K., Yamada, S., & Suzuki, H. 2008, ApJ, 688, 1176
Sumiyoshi, K., Yamada, S., Suzuki, H., & Chiba, S. 2006, PhRvL, 97, 091101
Summa, A., Hanke, F., Janka, H.-T., et al. 2016, ApJ, 825, 6
Suwa, Y., Sumiyoshi, K., Nakazato, K., et al. 2019, ApJ, 881, 139
Takiwaki, T., & Kotake, K. 2018, MNRAS, 475, L91
Takiwaki, T., Kotake, K., & Suwa, Y. 2016, MNRAS, 461, L112
Tchekhovskoy, A., McKinney, J. C., & Narayan, R. 2007, MNRAS, 379, 469
Toro, E. 2009, Riemann Solvers and Numerical Methods for Fluid Dynamics: A Practical Introduction (Berlin: Springer)
Torres-Forné, A., Cerdá-Durán, P., Obergaulinger, M., Müller, B., & Font, J. A. 2019a, PhRvL, 123, 051102
Torres-Forné, A., Cerdá-Durán, P., Passamonti, A., & Font, J. A. 2018, MNRAS, 474, 5272
Torres-Forné, A., Cerdá-Durán, P., Passamonti, A., Obergaulinger, M., & Font, J. A. 2019b, MNRAS, 482, 3967
Ugliano, M., Janka, H.-T., Marek, A., & Arcones, A. 2012, ApJ, 757, 69
van der Walt, S., Colbert, S. C., & Varoquaux, G. 2011, CSE, 13, 22
Vartanyan, D., Burrows, A., & Radice, D. 2019, MNRAS, 489, 2227
Vartanyan, D., Burrows, A., Radice, D., Skinner, M. A., & Dolence, J. 2018, MNRAS, 477, 3091
Westernacher-Schneider, J. R., O'Connor, E., O'Sullivan, E., et al. 2019, PhRvD, 100, 123009
Yakunin, K. N., Mezzacappa, A., Marronetti, P., et al. 2015, PhRvD, 92, 084040
Yasin, H., Schäfer, S., Arcones, A., & Schwenk, A. 2020, PhRvL, 124, 092701